Collection 6.1 MODIS Global Reservoir Product Algorithm Theoretical Basis Document (ATBD)

Version 1.0

Gang Zhao[1,2], Yao Li[1], Shuai Zhang[3], Deep Shah[1], Huilin Gao[1*]

[1] Department of Civil and Environmental Engineering, Texas A&M University

[2] Department of Global Ecology, Carnegie Institution for Science

[3] College of Marine Science, University of South Florida

Contact: hgao@civil.tamu.edu

Table of Contents

1. Introduction

Reservoirs serve as a lifeline in water management (e.g., irrigation, hydropower generation, water supply, and flood control), especially under the ongoing fast population growth and changing climate (Biemans et al. 2011; Cooke et al. 2016; Plate 2002; Schewe et al. 2014; Veldkamp et al. 2017). Globally, reservoirs supply about 40% of the total irrigation water demand (Biemans et al. 2011) and contribute to more than 60% of renewable energy via hydroelectricity (Murdock et al. 2019). Reservoir storage varies according to natural climate variability as well as the human water use/demand for different sectors (i.e., domestic, agricultural, and industrial). On one hand, near real-time reservoir storage monitoring is essential for mitigating the negative effects of hydro-climatic extremes (droughts and floods) (Mehran et al. 2015; Zhou 2020). On the other hand, long term records of water retained by global reservoirs can help to evaluate the human impacts on global and regional water cycles (Yigzaw et al. 2018; Zhou et al. 2016). However, because gauge observations for reservoir storage (and/or elevation) are typically not shared, both of the aforementioned data needs are difficult to satisfy at regional and global scales.

Among the reservoir water budget terms, reservoir evaporation accounts for a substantial amount of the loss of available water—particularly for reservoirs in arid/semi-arid regions (Friedrich et al. 2018). For example, the evaporation volume of Lake Tahoe (located in the western U.S.) represents 40%–60% of the total reservoir output (Friedrich et al. 2018). The annual evaporation rate of Lake Mead is ~1800 mm/year (Moreo 2015), which greatly exceeds the surrounding evapotranspiration rate (~50 mm/year) (Mu et al. 2011). At a regional scale, the water losses due to evaporation for 200 reservoirs in Texas are equivalent to 20% of their active storage value (Zhang et al. 2017). Thus, it is crucial to incorporate information about reservoir evaporation losses into existing water management practices. Nonetheless, because reservoir evaporation information obtained through reliable in situ measurements (e.g., eddy covariance, energy balance) is hard to acquire, pan evaporation data (which is less accurate due to the lack of consideration of heat storage and fetch effects) have been commonly used as an approximation (Friedrich et al. 2018). For most developing countries, even data about pan evaporation (or its equivalent) are not available.

This is the Algorithm Theoretical Basis Document (ATBD) for the global Moderate Resolution Imaging Spectroradiometer (MODIS) reservoir product. The reservoir product is available at two temporal resolutions: 8-day (MxD28C2) and monthly (MxD28C3). Here, MxD stands for

the fact that the product comes from both Terra (MOD) and Aqua (MYD) satellites. The objectives of this ATBD are: (1) to give a brief review of the current methods used for monitoring reservoirs using satellite observations; (2) to describe the MODIS reservoir algorithms, which are used to generate the product at two temporal resolutions (i.e., 8-day and monthly); (3) to introduce the required input datasets and parameters; (4) to show the validation results for that reservoir area, elevation, storage, and evaporation rate; and (5) to discuss the sources of product uncertainty.

2. Overview and Technical Background

Satellite remote sensing provides an alternative for filling in such reservoir data gaps. Since the 1990s, satellite radar altimeters have been utilized to measure the water levels of large lakes and reservoirs (Birkett 1995). To date, several databases have been developed to monitor the water levels of inland water bodies at a global scale—including the Global Reservoir and Lake Monitor (G-REALM) (Birkett et al. 2011), the Hydroweb database (Crétaux et al. 2011), and the Database for Hydrological Time Series of Inland Waters (DAHITI) (Schwatke et al. 2015). Meanwhile, the global surface area variations of lakes and reservoirs have been assessed from various satellite instruments, such as the Landsat and MODIS (Donchyts et al. 2016; Khandelwal et al. 2017; Ling et al. 2020; Pekel et al. 2016; Yao et al. 2019; Zhao and Gao 2018). Pekel et al. (Pekel et al. 2016) developed a Global Surface Water (GSW) dataset using expert system classifiers based on Landsat observations obtained over the last three decades. The more recently published Global Reservoir Surface Area Dataset (GRSAD) provides monthly water area values for over 7000 reservoirs (Zhao and Gao 2018), which were generated by correcting the underestimations due to cloud contamination in the GSW dataset. Khandelwal et al. (Khandelwal et al. 2017) generated 8-day composite water area time series datasets for 94 reservoirs using MODIS multispectral data at 500 m resolution. In the meantime, many studies have focused on generating satellite-based reservoir storage estimations by combining elevation and area observations collected from multiple missions (Busker et al. 2019; Crétaux et al. 2011; Gao et al. 2012; Zhang et al. 2014). For example, Gao et al. (Gao et al. 2012) monitored storage values for 34 global reservoirs from 1992 to 2010 by combining water surface areas from MODIS with water elevations from satellite radar altimetry (which represented 15% of the total global reservoir capacity during that period). The Hydroweb database (http://hydroweb.theia-land.fr/) estimates the storage changes for about 60 large lakes and reservoirs beginning in 1992, using multi-source satellite imagery (e.g., MODIS and Landsat) and radar altimetry data (Crétaux et al. 2011). More recently, Busker et al.

(Busker et al. 2019) analyzed the monthly volume variations between 1984 and 2015 for 137 lakes and reservoirs at a global scale by combining water area values from the GSW dataset (Pekel et al. 2016) and elevation values from DAHITI (Schwatke et al. 2015).

Meanwhile, some new approaches have been recently developed to estimate evaporation rates and losses from space. For instance, Zhang et al. (2017) estimated the monthly evaporation volumes based on pan-derived evaporative rates and Landsat surface areas for more than 200 reservoirs in Texas. Zhao and Gao (2019) used the Penman Equation (with the heat storage and fetch effects addressed), and generated a first long-term evaporation data record for over 700 reservoirs in the Contiguous United States. Zhao et al. (2020) further improved the calculation of the heat storage change term by leveraging MODIS surface temperature data. Many other approaches were developed and tested at individual locations (Althoff et al. 2019; Meng et al. 2020; Mhawej et al. 2020).

Despite the development of remotely sensed reservoir datasets, consistent, comprehensive, long-term, and operationally monitored reservoir products are still lacking at the global scale. Therefore, the newly developed NASA global MODIS water reservoir product (MxD28) can fill in this knowledge gap.

3. MxD28 Algorithm Descriptions

The MxD28C2 product includes the reservoir area, elevation, and storage results at 8-day temporal resolution. Figure 1 shows the flowchart for generating the MxD28C2 product. The algorithms corresponding to both products are explained in the following sections. First, the 8-day reservoir area values were extracted from the 250-m Near Infrared (NIR) band of MODIS Terra/Aqua surface reflectance (MxD09Q1) data. Then, the area values were applied to the Area-Elevation (A-E) relationship for the given reservoir provided by the GRBD (Li et al. 2020) to calculate the corresponding elevation values. Lastly, the reservoir storage was estimated after Gao et al. (2012).

Figure 1. Flow chart of the algorithm for deriving the MxD28C2 (8-day) product. The green boxes represent the product components.

The MxD28C3 product includes the evaporation rate and volumetric evaporation loss in addition to the area, elevation, and storage results at monthly temporal resolution. Figure 2 shows the flowchart for generating the MxD28C3 monthly product. The monthly area values were first estimated based on the composite of the 8-day area classifications, and then converted to monthly elevation and storage results using the A-E relationship (Figure 2). In addition, monthly evaporation rates were estimated after the Lake Temperature and Evaporation Model (LTEM) (Zhao et al. 2020) using MODIS LST product (MxD21A2) and meteorological data from the Global Land Data Assimilation System (GLDAS) (Rodell et al. 2004). Lastly, the monthly evaporative volumetric losses were calculated as the product of evaporation rate and reservoir area values.

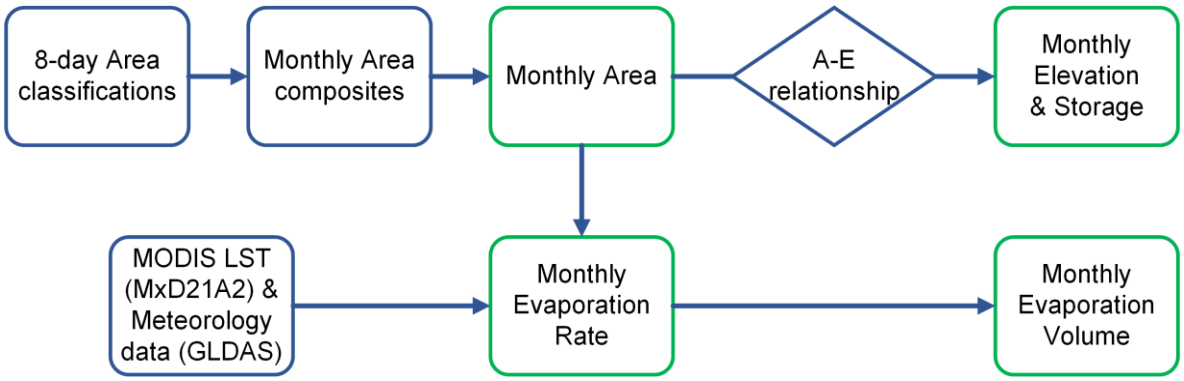

Figure 2. Flow chart of the algorithm for deriving the MxD28C3 product, which contains monthly area, elevation, storage, evaporation rate, and volumetric evaporation loss results for the 164 reservoirs. The green boxes represent the product components.

The detailed algorithms for generating reservoir area, elevation, storage, evaporation rate, and evaporation volume are explained in the following subsections.

3.1 Algorithms for reservoir area

3.1.1 Algorithm for MxD28C2 (8-day Product)

The algorithm for estimation of reservoir area is explained using the following steps (as illustrated in Figure 3).

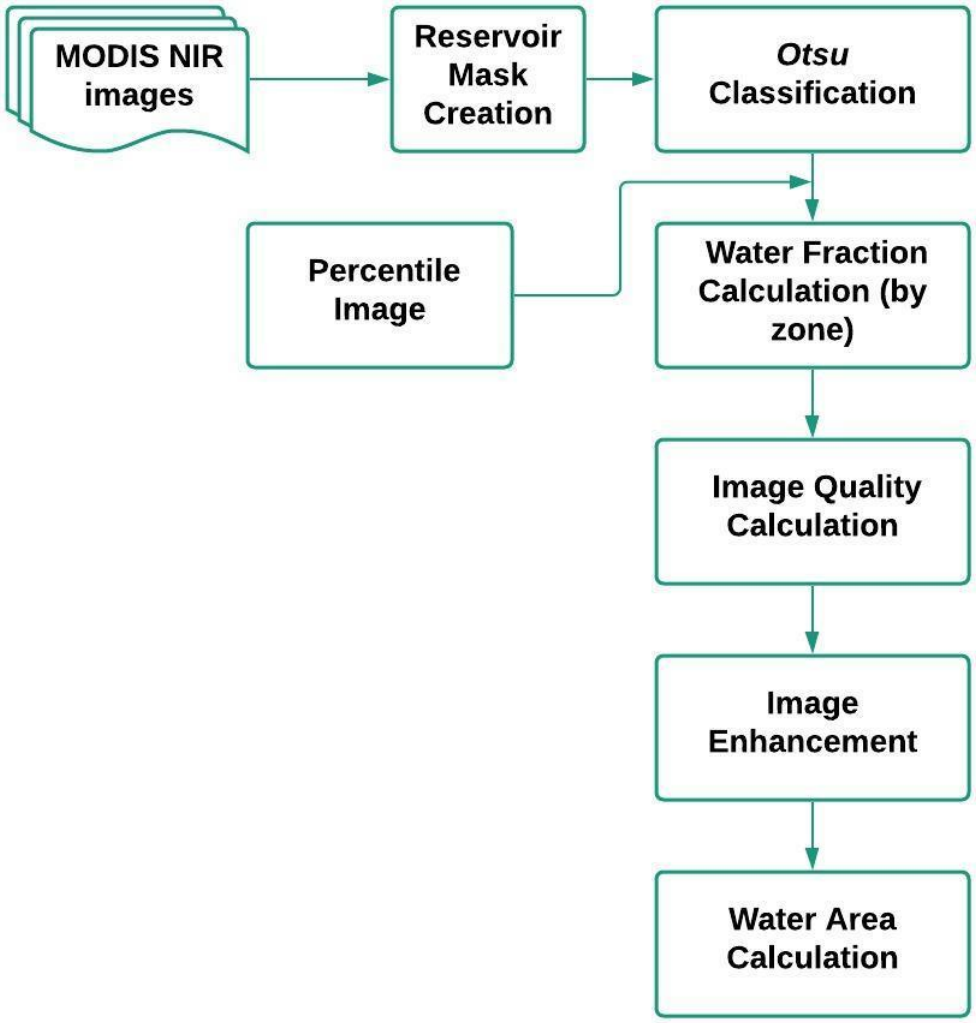

Figure 3. Flowchart for the the Image Enhancement Algorithm.

1. **Mask creation:** For a given reservoir of interest, the shapefiles from HydroLAKES (Messager et al. 2016) and OpenStreetMap (Haklay and Weber 2008) were compared and the one with the larger area was selected. By leveraging these two shapefile datasets, the possible underestimations from either of them can be eliminated. It should be noted that we manually corrected some polygons that were found to have large discrepancies from Google maps. These alterations are reported in Li et al. (2020). The reservoir mask was then generated by buffering the selected shapefile outward by 1000 m. This buffering approach allowed the mask to include all possible water pixels (Gao et al. 2012). All of the subsequent steps were executed within the masked region.
2. **Otsu classification.** For each of the MODIS NIR image, the contaminated pixels (i.e., cloud, cloud shadow, or snow/ice) were removed by using the quality assurance (QA) band

of MOD09Q1. Then, the Otsu thresholding method (Otsu 1979) was applied to the clear pixels for classifying the raw water area.

3. **Enhancement decision.** The contamination percentage (CP) were calculated for each image using the number of contaminated pixels divided by the total number of pixels inside of the reservoir mask. If CP ≥ 60%, which indicating severe contamination of the NIR image, the raw water area was discarded and the water area was reported as a "missing" value (i.e., -9999). If CP < 15%, the image was regarded as clear image and the raw water area was reported as the final water area for this 8-day timeframe. Otherwise (15% ≤ CP <60%), the following enhancement algorithm was performed.
4. **Percentile image creation.** The surface water occurrence (value ranges from 0% to 100%) image from global surface water dataset (GSWD; Pekel et al. (2016)) was resampled from its original 30m resolution to MODIS 250m resolution. Then it was grouped into 50 zones based on the occurrence values, using a fixed increment percentile value of 2%. This threshold (of 2%) allowed us to narrow down the differences among pixels within a given zone. In other words, all the pixels within the same zone indicate that they have a similar possibility of being classified as water.
5. **Water fraction calculation (by zone):** Zonal water coverage maps are created for each classification image overlaying the percentile mask image on it (shown in Figure 4, rows a and b). The percentage of water pixels within each zone is calculated using Equation (1):

$$p_i = \frac{n_i}{N_i}, \quad i = 1, 2, \dots, k \tag{1}$$

where n_i is the number of pixels in the i^{th} zone that are classified as water (according to the MODIS NIR classification), N_i is the total number of pixels in the i^{th} zone (according to the delineation of the percentile image), and k is the total number of zones. In the simplification example, the p_i value for zone 1, zone 2, and zone 3 are 15/16, 6/9, and 0/3, respectively.

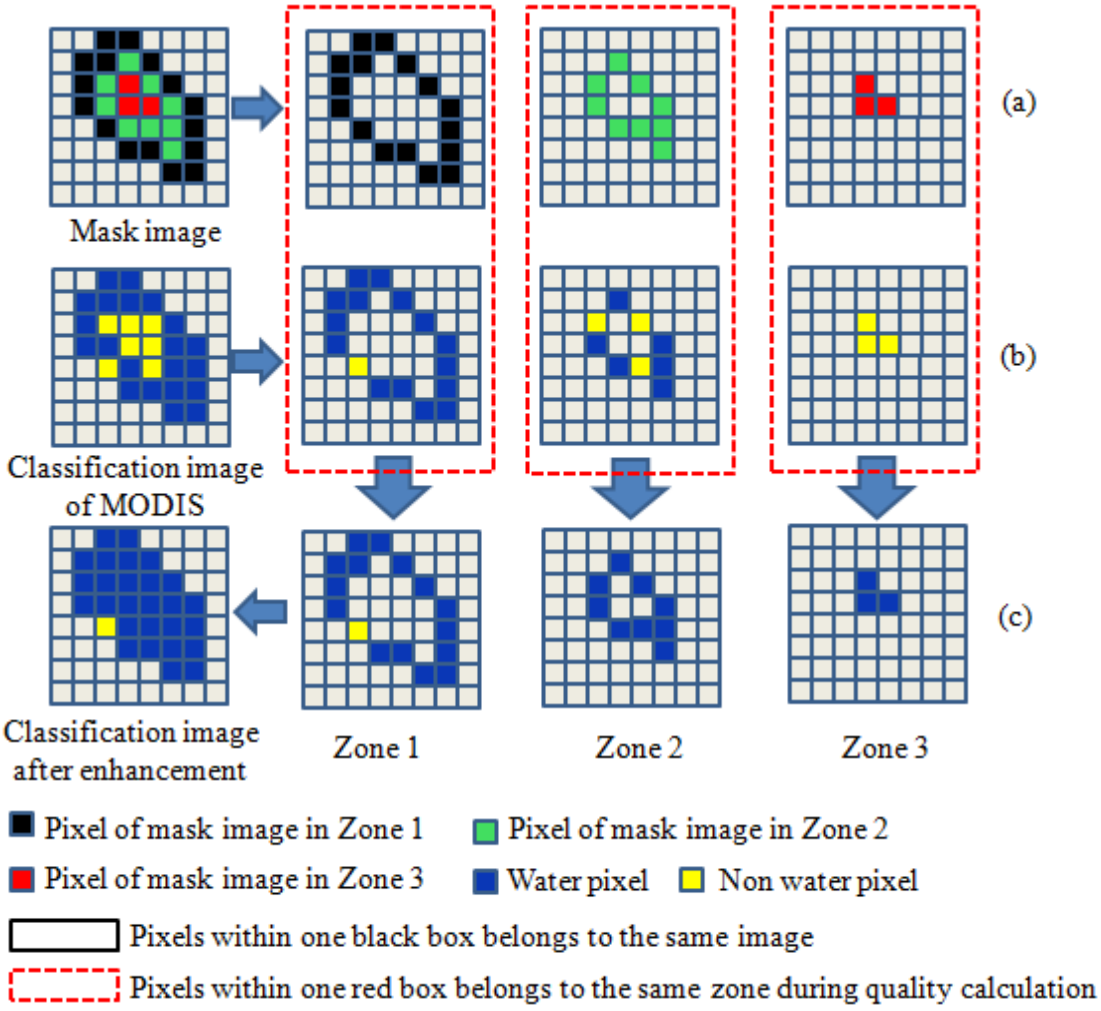

Figure 4. A simple example showing the classification image enhancement process: (a) dividing the mask file into multiple zones (i.e., three zones in this example); (b) assigning zone values to the classified image; and (c) enhancing the classified image based on image quality.

6. **Image quality assessment:** A quality parameter (Q) is computed for each classification image according to Equation (2).

$$Q = \frac{\sum_{i=1}^{k}(p_i - 0.5)^2}{k} \quad (2)$$

Q is a measure of the overall consistency of the surface water classification from a MODIS NIR image. Given p_i is from 0 to 1, Q has a range between 0 to 0.25. The Q value increases as the quality of a water classification image increases. If a classification is of high quality, then the p_i values for the zones classified as water should be 1 (or close to 1), while the p_i values for the zones classified as land should be zero (or close to zero). In the case of an ideal classification (i.e., p_i equal or close to 1 or 0 for all i values), the Q value is close to

the maximum (0.25). In contrast, if a classification image is of very low quality, the p_i values for most of the zones should be close to 0.5 (0.5 represents the case of a random distribution of water pixels within a zone). As a result, the Q value is close to zero for a low-quality image. For the sample classification illustrated in Figure 4, its Q value equals to 0.156.

7. **Classification image enhancement**: For each zone (i = 1, 2, …, k) within one classification image, if its p_i value is larger than a threshold T, then all pixels in the j^{th} zone (j ranges from $i+1$ to k) are set as water. The threshold T is determined according to equation (3):

$$T = \begin{cases} C_p & Q > C_Q \\ p_m & Q \leq C_Q \end{cases} \quad (3)$$

where p_m is the median of all the p_i values within one classification image, and C_p and C_Q are each constant parameters. The threshold value T for each image is based on its quality Q: if Q is larger than C_p, then T is equal to C_p; otherwise, T equals p_m. Calibrated over two reservoirs where observations are available (i.e., the Pong and Hirakud reservoirs), C_p and C_Q are set to 0.7 and 0.1, respectively. The enhancement process for this simplified example is illustrated in Figure 4 (row c). Given that the Q value (Q = 0.156) of the classification image is larger than C_Q (C_Q=0.1), the threshold T is set to 0.7. For this classification image, since p_1 (p_1 = 0.94) is larger than T (T = 0.7), all pixels in zone 2 and zone 3 are assigned as water.

This classification image enhancement is based on two principles. First, a good classification image should have good consistency—meaning pixels in the same zone should have the same classification results. Second, pixels in the zones with a higher percentile should have a greater possibility of being classified as water than those in zones with lower percentile values. This means that if the probability that a zone is covered by water exceeds the threshold T (as defined in Equation (3)) all pixels of the remaining inner reservoir zones are labeled as water.

3.1.2 Algorithm for MxD28C3 (Monthly Product)

The monthly enhanced area values were estimated similarly as 8-day product but based on the composite of the 8-day area classifications. A pixel was assigned as a water pixel if this pixel was classified as water in any of the 8-day images within this month. This “max” composite approach might slightly overestimate the monthly mean water area value. However, given that

the water area variation within a month is relatively small for large reservoirs (except when there is flooding), the monthly area time series can adequately represent the long-term dynamics of the reservoir.

3.2 Algorithms for reservoir elevation and storage

The enhanced area values (A_{MODIS}) were applied to the Area-Elevation (A-E) relationship (Equation (4)) to calculate the corresponding elevation values (h_{MODIS}). For each given reservoir, the A-E relationship function, $f()$, was adopted from the Global Reservoir Bathymetry Dataset (GRBD; Li et al. (2020)).

$$h_{MODIS} = f(A_{MODIS}) \tag{4}$$

The corresponding reservoir storage can be estimated using Equation (5) (after Gao et al. (2012)):

$$V_{MODIS} = V_c - (A_c + A_{MODIS})(h_c - h_{MODIS})/2 \tag{5}$$

where V_c, A_c, and h_c represent storage, area, and water elevation values at capacity; and V_{MODIS}, A_{MODIS}, and h_{MODIS} are the estimated storage, area, and water elevation from MODIS.

3.3 Algorithms for evaporation rate and evaporation volume

The detailed algorithm for the evaporation rate and volumetric evaporation loss (for MxD28C3) is explained in following sections.

3.3.1 Generating water surface temperature (WST) value

Similar to the monthly water area calculation, the WST value for each month was calculated using the monthly composite of 8-day LST images (i.e., MOD21A2 and MYD21A2). For each month, a composite image was first created by averaging the 8-day LST images in this month. Then, the two bands (daytime LST and nighttime LST) were averaged to generate the monthly mean LST image. Since the daily temperature variations roughly follow a sinusoidal curve, the average of the MODIS daytime and nighttime temperatures (1:30/13:30 local time for Aqua and 10:30/22:30 for Terra) can effectively represent the mean daily temperature.

The reservoir average WST was then calculated by averaging the LST pixel values that overlap with the raw water area (generated in Section 3.1.2). Because the raw water area has a resolution of 250m and LST image has a resolution of 1km, the raw water area image was up-scaled to 1km resolution: For each 1km pixel (overlapping with 16 pixels in 250m resolution),

the percentage of water area inside of this pixel was calculated. For example, if there are 9 pixels out of 16 in the 250m image is classified as water, then the water area percentage of this 1km pixel is 9/16 = 56.25%. In order to reduce the impacts of mixed pixel in the LST image on the average WST value, we only selected the 1km pixels that have water area percentage greater than or equal to 75% (i.e., at least 12 water pixels in 250m resolution).

3.3.2 Calculating evaporation rate time series using LTEM

The evaporation rate calculation in LTEM is based on the Penman equation, with the wind function represented after Zhao and Gao (2019) (Equation 6):

$$E = \frac{\Delta(R_n - G) + \gamma f(u)(e_s - e_a)}{\lambda_v(\Delta + \gamma)} \quad (6)$$

where E is the open water evaporation rate ($mm \cdot d^{-1}$); Δ is the slope of the saturation vapor pressure curve ($kPa \cdot °C^{-1}$); R_n is the net radiation ($MJ \cdot m^{-2} \cdot d^{-1}$); G is the heat storage change of the water body ($MJ \cdot m^{-2} \cdot d^{-1}$); γ is the psychrometric constant ($kPa \cdot °C^{-1}$); $f(u)$ is the wind function that is dependent on reservoir fetch ($MJ \cdot m^{-2} \cdot d^{-1} \cdot kPa^{-1}$) (McJannet et al. 2012); e_s is the saturated vapor pressure at air temperature (kPa); e_a is the air vapor pressure (kPa); and λ_v is the latent heat of vaporization ($MJ \cdot kg^{-1}$). The Penman equation and its variants (e.g., the Penman-Monteith equation) have been widely employed for potential evapotranspiration as well as for open water evaporation estimations (McJannet et al. 2008; McMahon et al. 2013; Tanny et al. 2008).

However, there are two key factors that need to be considered when applying the Penman equation to open water evaporation estimation. The first is associated with the meteorological data that are used to drive the Penman equation. Ideally, the meteorological data should be directly collected over the water surface. However, due to the difficulties, logistics, and costs associated with acquiring measurements over water, most studies have employed land-based meteorological data as a substitute (Dos Reis and Dias 1998; McJannet et al. 2012; Winter et al. 1995). Direct use of land-based meteorological data in the Penman equation is likely to result in a biased estimation, given the meteorological differences between land and water areas (Weisman and Brutsaert 1973). Specifically, when air moves from land across the water body, its humidity gradually increases due to the evaporation processes on the water surface. This will lead to decreasing evaporation fluxes in the downwind direction.

To solve this problem, McJannet et al. (2012) developed a generally applicable wind function that facilitates the open-water evaporation rate calculation using standard land-based meteorology. This empirical function uses a fetch length to include the effect of air becoming moister when moving from land to water surface (Equation 7):

$$f(u_2) = \lambda_v(2.33 + 1.65u_2)L_f^{-0.1} \quad (7)$$

where $f(u_2)$ is the wind function ($MJ \cdot m^{-2} \cdot d^{-1} \cdot kPa^{-1}$); u_2 is the wind speed at the height of 2 m ($m \cdot s^{-1}$); and L_f is the fetch length of the water body (m). The coefficients in Equation 7 were identified by regressing u_2 and L_f against data from 19 previously published wind functions, which represent a range of water bodies with various sizes and climate conditions (McJannet et al. 2012). Because the wind speed values from reanalysis datasets are generally reported at a 10-m height, they were converted to 2-m values using the standard grass surface roughness (Allen et al. 1998). Open water roughness was not used in order to be consistent with the generalized wind function from (McJannet et al. 2012).

The fetch length was calculated for each reservoir and each month (Figure 5). With a given wind direction (monthly dominant wind direction derived from NCEP/NCAR Reanalysis data; Kalnay et al. (1996)), the width is defined as the distance between the two reservoir-tangent lines that are parallel to the wind direction. Then fetch length was calculated by dividing the total area with the width.

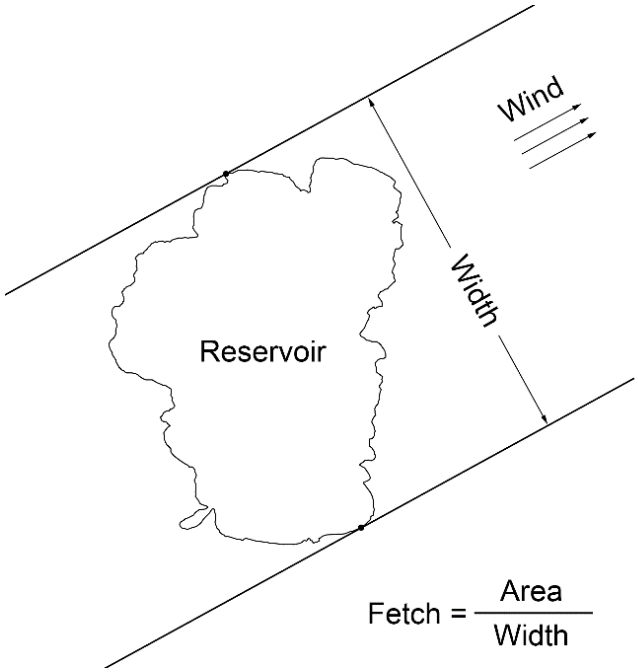

Figure 5. Calculation of the reservoir fetch for a given wind direction.

The second key factor to be considered when applying the Penman equation to open water evaporation is the heat storage quantification. For instance, reservoirs tend to store heat in the spring/summer and release heat in the fall/winter. Without considering this heat storage effect, the evaporation rate would be overestimated in the former and underestimated in the latter.

In the following sub-sections (3.3.2.1 to 3.3.2.3), we focused on explaining the new approach for quantifying the heat storage change term that leverages MODIS WST data. The heat storage changes (G) can be calculated using temperature profile data for two consecutive time steps (Equation 8; Gianniou and Antonopoulos (2007)):

$$G = \frac{1}{A_s}\frac{\mathrm{d}}{\mathrm{d}t}\int_0^{D_t} \rho_{w,z,t} c_{w,z,t} A_{z,t} T_{z,t}\, \mathrm{d}z \tag{8}$$

where A_s is the surface area of the water body (m^2); t is the current time step (d); $\rho_{w,z,t}$ is the density of water at depth z and time t ($kg \cdot m^{-3}$); $c_{w,z,t}$ is the specific heat of water at depth z and time t ($J \cdot kg^{-1} \cdot °C^{-1}$), $A_{z,t}$ is the water area at depth z and time t (m^2); $T_{z,t}$ is the water temperature at depth z and time t (°C); and D_t is the total depth of the water body at time t (m).

To simulate the temperature profile for each time step ($T_{z,t}$, $0 \le z \le D_t$ and $0 \le t \le END$) in LTEM, we integrated MODIS WST data into the 1-D Hostetler Model (Hostetler and Bartlein 1990). In this subsection, we first explain the reservoir energy budget terms (3.3.2.1) and then the Hostetler Model (3.3.2.2), which were used to facilitate temperature profile and evaporation rate simulation in LTEM (3.3.2.3).

3.3.2.1 Reservoir energy budget terms

The evaporation process of a reservoir involves both energy fluxes at the water surface and energy transfer in the water body (Figure 6).

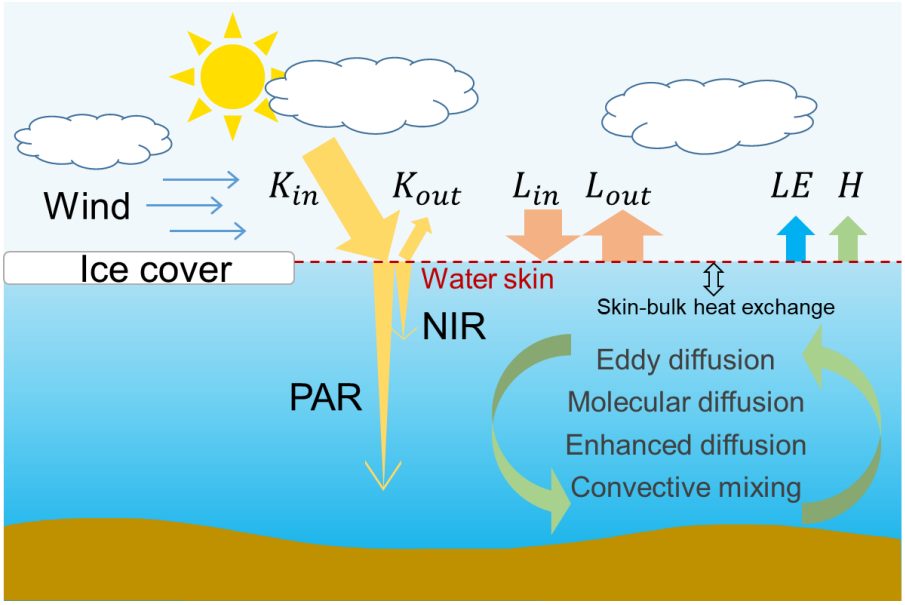

Figure 6. Schematic of the Lake Temperature and Evaporation Model (LTEM) model, which involves both energy fluxes at the water surface and energy transfer in the water body. PAR and NIR represent photosynthetically active radiation and near infrared radiation, respectively. Definitions for other energy terms can be found in Equations 9 and 16.

For a water body, the net radiation (R_n, MJ·m^{-2}·d^{-1}) can be formulated after Equation 9:

$$R_n = K_{in} - K_{out} + L_{in} - L_{out} \tag{9}$$

where K_{in}, K_{out}, L_{in}, and L_{out} are surface incoming shortwave radiation (MJ·m^{-2}·d^{-1}), outgoing shortwave radiation (MJ·m^{-2}·d^{-1}), surface incoming longwave radiation (MJ·m^{-2}·d^{-1}), and outgoing longwave radiation (MJ·m^{-2}·d^{-1}), respectively. Among these terms, K_{in} can be directly adopted from meteorological forcing inputs, while the others are calculated. K_{out} can be calculated using the water surface albedo (α) following Equation 10 after (Subin et al. 2012):

$$K_{out} = \alpha \cdot K_{in} = \frac{0.05}{\cos\theta_s + 0.15} \cdot K_{in} \tag{10}$$

where θ_s is the solar zenith angle (Zhao and Gao 2019). L_{in} (MJ·m^{-2}·d^{-1}) and L_{out} (MJ·m^{-2}·d^{-1}) can be calculated using Equations 11 and 12 after the Stefan–Boltzmann Law:

$$L_{in} = \varepsilon_a \sigma (T_a + 273.15)^4 \tag{11}$$

$$L_{out} = \varepsilon_w \sigma (WST + 273.15)^4 \tag{12}$$

where ε_a is the emissivity of air with a cloudiness factor included (0-1; Zhao and Gao (2019)); ε_w is the emissivity of water (0.97); σ is the Stefan-Boltzman constant (4.9×10^{-9} MJ·m^{-2}·K^{-4}·d^{-1}); and T_a is the air temperature (°C).

The net shortwave radiation ($K_{in} - K_{out}$) penetrates the water column and is absorbed according to the Beer-Lambert Law. The net shortwave radiation is divided into photosynthetically active radiation (PAR) and near-infrared radiation (NIR). The transmitted shortwave energy at depth z (denoted as K_z) can be calculated after Equation 13 (Ingle Jr and Crouch, 1988):

$$K_z = (K_{in} - K_{out}) \cdot \left(\theta_{PAR} e^{-\lambda_{PAR} \cdot z} + \theta_{NIR} e^{-\lambda_{NIR} \cdot z}\right) \quad (13)$$

where θ_{PAR} and θ_{NIR} are the shortwave radiation fractions of PAR and NIR; and λ_{PAR} and λ_{NIR} are the light attenuation coefficients of PAR and NIR. After Escobedo et al. (2009), θ_{PAR} and θ_{NIR} are set to 0.54 and 0.46, respectively. λ_{NIR} is set to 1.4 m^{-1} after Bowling and Lettenmaier (2010). The λ_{PAR} value is provided by the user when direct light attenuation measurements are available, or it can be calculated from the Secchi depth measurement (Z_{sd}, in m) using Equation 14 (Devlin et al. 2008). Alternatively, λ_{PAR} can be empirically calculated using the lake/reservoir average depth (D, in m) after Equation 15 (Bennington et al. 2014; Håkanson 1995). Because Secchi depth data is not available at a global scale (for all the 164 reservoirs), we used Equation 15 here for calculating λ_{PAR}.

$$\lambda_{PAR} = exp(0.253 - 1.029 \cdot lnZ_{sd}) \quad (14)$$

$$\lambda_{PAR} = 1.1925 D^{-0.424} \quad (15)$$

Unlike shortwave radiation which can penetrate water, the incoming longwave radiation (L_{in}) is only absorbed by the water surface. Meanwhile, the surface also loses energy through outgoing longwave radiation (L_{out}), latent heat flux (LE, MJ·m^{-2}·d^{-1}), and sensible heat flux (H, MJ·m^{-2}·d^{-1}). In summary, for a given water body, the energy it receives can be separated into two parts based on location: 1) the "penetrating" net shortwave radiation ($K_{in} - K_{out}$), and 2) the "surface" energy influx (EI_s) which is defined after Equation 16:

$$EI_s = L_{in} - L_{out} - LE - H \quad (16)$$

3.3.2.2 The Hostetler Model

To facilitate the calculation of temperature profile, the modified Hostetler Model scheme was adopted from Bowling and Lettenmaier (2010) and Subin et al. (2012). The governing equation for water temperature profile is denoted as a partial differential equation (Equation 17):

$$\frac{\partial T_{z,t}}{\partial t} = \frac{1}{A_{z,t}} \frac{\partial}{\partial z} \left[A_{z,t} (\kappa_m + \kappa_{E,z,t} + \kappa_{en}) \frac{\partial T_{z,t}}{\partial z} \right] + \frac{1}{A_{z,t}} \frac{1}{c_{w,z,t}} \frac{\partial \left(K_{z,t} A_{z,t} \right)}{\partial z} \tag{17}$$

where $T_{z,t}$ is the water temperature at depth z and time t; κ_m is the molecular diffusivity (1.39×10^{-7} $m^2 \cdot s^{-1}$); $\kappa_{E,z,t}$ and κ_{en} are the eddy and enhanced diffusivities, respectively ($m^2 \cdot s^{-1}$); $K_{z,t}$ is K_z (Equation 13) at time t; and $A_{z,t}$ is the area at depth z and time t (which is calculated using the reservoir bathymetry). Following Hostetler and Bartlein (1990), $\kappa_{E,z,t}$ can be calculated after Equation 18:

$$\kappa_{E,z,t} = \frac{(\kappa v_s z / P_0) e^{-k_e z}}{1 + 37 R_i^2} \tag{18}$$

where κ is the von Kármán constant (0.4); v_s is the surface shear velocity (which depends on surface forcing and temperature; Vickers et al. (2015)); P_0 is the neutral value of the turbulent Prandtl number (1.0); k_e is the Ekman profile parameter; and R_i is the gradient Richardson number. The detailed formulation for these parameters can be found in Hostetler and Bartlein (1990).

The enhanced diffusion is introduced by turbulence sources other than wind-driven eddies, such as surface water inflow/outflow, seiches, the horizontal temperature gradient, and aquatic life movement. κ_{en} can be written as Equation 19:

$$\kappa_{en} = \alpha_\kappa \cdot 1.04 \times 10^{-8} (N^2)^{-0.43} \tag{19}$$

where α_κ is the enhanced diffusion coefficient ($0 \leq \alpha_\kappa \leq 1000$; Bennington et al. (2014)), and N^2 is the Brunt-Vaisala frequency (s^{-2}) (Fang and Stefan 1996; Subin et al. 2012). The value of α_κ can be calibrated using temperature profile measurements (Ellis et al. 1991). We used an empirical value of 20 for α_κ for this MODIS product. We did, however, test the sensitivity of α_κ (using Lake Mead as an example) to find its impacts on the temperature profile and the evaporation rate (Section 4.4 of Zhao et al. (2020)).

For general Hostetler Model applications, the water temperature profiles are calculated after Equation 17 with $K_{in} - K_{out}$ and EI_s as energy inputs. Then, the convection is implemented

from the top layer to the bottom according to the temperature-based density gradient. For instance, if an upper layer is denser than its adjacent lower layer (density calculated based on temperature), then these two layers will be mixed and the resulting thickness-weighted average temperature will be assigned to both of them. This convection process is executed until there is no inverse density gradient.

3.3.2.3 Reservoir temperature profile and evaporation simulation

The process at each time step is summarized in the following 6 steps (and in the flowchart in Figure 7):

1. Prior to the iteration at the current time step (t), it was first assumed that there is no heat storage effect in the Penman equation (i.e., G = 0 in Equation 6). Thus, an initial value of EI_s can be calculated, with $LE = \lambda_v E$ and H calculated after Equation 20 (with the same wind function as used in Equation 6):

$$H = \gamma f(u)(WST_t - T_a) \tag{20}$$

2. $T_{z,t}$ ($0 \le z \le D_t$) can then be calculated using the Hostetler Model based on $T_{z,t-1}$ ($0 \le z \le D_{t-1}$), along with $K_{in} - K_{out}$, EI_s, and the layer configuration derived from the reservoir bathymetry. For the current version of the calculation, the reservoir bathymetry was assumed to be cylindrical to avoid the impacts of reservoir sediment heating—meaning the radiative energy will be trapped in the bottom instead of reflecting back in the shallow reservoirs.

3. The remotely sensed skin temperature at time t (WST_t) was converted to the bulk temperature (T_t^{bulk}) by considering the cool-skin effect ($\Delta T_{skin,t}$) after Equation 21 (Artale et al. 2002). Compared to the more complex formulation provided by Fairall et al. (1996), the formulation by (Artale et al. 2002) significantly simplifies the computation and still produces satisfactory outputs (Tu and Tsuang 2005).

$$T_t^{bulk} = WST_t + \Delta T_{skin,t} = WST_t + \frac{EI_s/0.0864 \cdot \delta}{k} \tag{21}$$

where δ is the thickness of the skin layer (m), and k is the thermal conductivity of water ($W \cdot m^{-1} \cdot K^{-1}$). This bulk temperature represents the water temperature of the first water layer right beneath the skin layer.

4. If the simulated $T_{0,t}$ was different from the remotely sensed T_t^{bulk}—which indicated that the initial EI_s was biased— Δ_{EI} was subtracted from EI_s, and Steps 2 and 3 were repeated. This iteration was executed until $\left|T_{0,t} - T_t^{bulk}\right|$ was smaller than ϵ (e.g., 0.01 °C). Δ_{EI} is defined as:

$$\Delta_{EI} = lr \cdot \left(T_{0,t} - T_t^{bulk}\right) \quad (22)$$

where lr is the learning rate (e.g., π, or other irrational numbers).

5. After the model had converged (i.e., $\left|T_{0,t} - T_t^{bulk}\right| < \epsilon$), the heat storage change (G) was calculated following Equation 8 (Gianniou and Antonopoulos 2007).

6. The evaporation rate (E) was then calculated using the Penman equation (with the wind function represented) after Equation 1 in Zhao and Gao (2019).

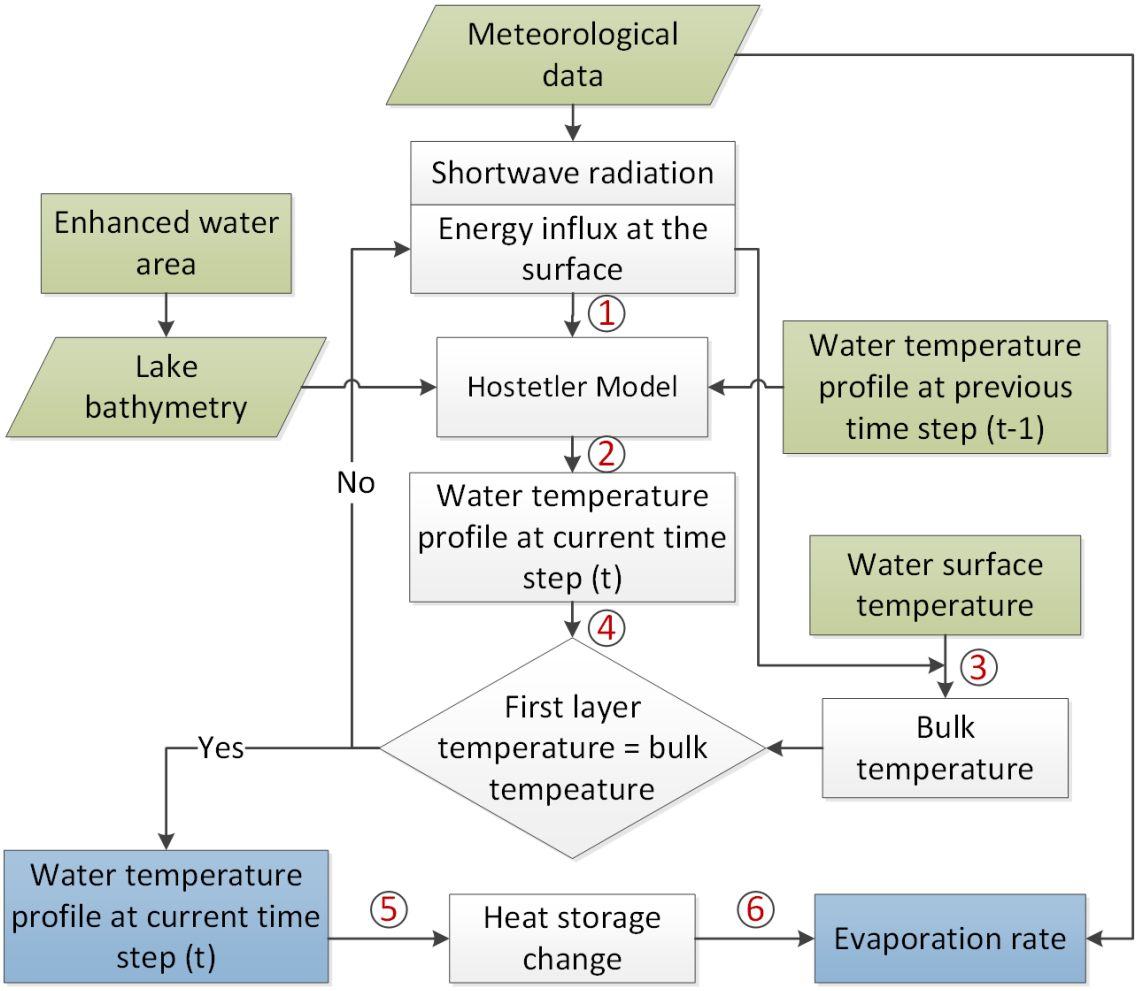

Figure 7. Flowchart for calculating the water temperature profile from $t-1$ to t, and the heat storage and evaporation rates. Green and blue colors indicate inputs and outputs, respectively.

In summary, by implementing the above iterations, the water temperature profile at the previous time step ($T_{z,t-1}$)—and the water skin temperature at the current time step (WST_t)—can lead to the water temperature profile at the current time step ($T_{z,t}$). To get a stable temperature profile time series, LTEM can be spun up for a sufficient period of time (e.g., 24-months), and then normal simulations can be started. We implemented LTEM at a monthly time step—meaning that we solved the temperature profile for each month, and then calculated the evaporation rate for each month.

3.3.3 Calculating volumetric evaporation

After calculating the evaporation rate time series, the volumetric evaporation can be inferred by multiplying the evaporation rate with the surface area (Equation 23).

$$V_E = E \times A \tag{23}$$

where E is the evaporation rate (mm/d) and A is the enhanced water area (km^2).

4. Input Datasets

The input datasets include three categories: reservoir shapefiles, input variables, and reservoir parameters. The details of these inputs can be found in the following sub-sections.

4.1 Reservoir shapefiles

The reservoir shapefiles were adopted from HydroLAKES (Messager et al. 2016) and OpenStreetMap (Haklay and Weber 2008). For a given reservoir, the two shapefiles were compared and the one with the larger area was selected. By leveraging these two shapefile datasets, the possible underestimations from either of them can be eliminated. It should be noted that we manually corrected some polygons that were found to have large discrepancies from Google maps. The purposes of the shapefiles are two-fold: for extracting the meteorological data over the reservoirs and for generating reservoir masks.

4.2 Input variables

The time varying input variables are from other MODIS products and meteorological data, which are summarized in Table 1.

Table 1. Summary of the input variable names, sources and purposes used in this study

Data	Spatial resolution	Temporal resolution	Purpose	Reference
Terra surface reflectance (MOD09Q1)	250 m	8-day	Water area extraction	Vermote (2015)
Aqua surface reflectance (MYD09Q1)	250 m	8-day	Water area extraction	Vermote (2015)
Terra LST (MOD21A2)	1 km	8-day	WST extraction	Hulley and Hook (2017)
Aqua LST (MYD21A2)	1 km	8-day	WST extraction	Hulley and Hook (2017)
GLDAS-2.1	0.25°	1-month	Meteorological forcing data for LTEM	Rodell et al. (2004); Beaudoing and Rodell (2020)

The land surface temperature contains day/night surface temperature for inland water areas.

(1) Inputs from other MODIS products

For MxD28C2, the 8-day Terra/Aqua surface reflectance (MxD09Q1) data were collected for water area extraction (Vermote 2015). Specially, only the near-infrared (NIR) band was used due to its high spatial resolution (i.e., 250 m for MODIS). The NIR band has been commonly utilized for the extraction of water bodies because it is strongly absorbed by water but scarcely absorbed by terrestrial dry soil and vegetation (McFeeters 1996). The A-E relationships were adopted from GRBD (Li et al. 2020), which have proven to be of high quality through validation against in situ data. Then, the 8-day water area estimations were applied to the A-E relationships to derive elevation and storage values. Moreover, we used the 8-day day/night land surface temperature (LST) products (MxD21A2; Hulley and Hook (2017)) and Global Land Data Assimilation System (GLDAS; Rodell et al. (2004)) meteorological forcing data to estimate the evaporation rates and volumes (see Section 3.3 for more detailed approach).

(2) Meteorological data

We obtained the meteorological data from the NASA Global Land Data Assimilation System Version 2.1 (GLDAS-2.1; Rodell et al. (2004); Beaudoing and Rodell (2020)) to drive the

LTEM. In this version GLDAS is forced with a combination of model and observation data from 2000 to present. For instance, it was forced with National Oceanic and Atmospheric Administration (NOAA)/Global Data Assimilation System (GDAS) atmospheric analysis fields (Derber et al. 1991), the disaggregated Global Precipitation Climatology Project (GPCP) precipitation fields (Adler et al. 2003), and the Air Force Weather Agency's AGRicultural METeorological modeling system (AGRMET) radiation fields which became available for March 1, 2001 onwards. We used monthly downward shortwave radiation (W/m2), air temperature (in K), specific humidity (in kg/kg), and wind speed (in m/s) data from Mar 2000 to present, with a spatial resolution of 0.25 degree to drive the LTEM. For any reservoir covering multiple GLDAS grids, the meteorological forcings were first averaged over those grids.

4.3 Reservoir parameters

The following reservoir parameters are used for generating the products: storage at capacity, elevation at capacity, surface area at capacity, A-E relationship, average reservoir depth, and average latitude. The detailed information for each reservoir is provided in appendix A. More details about the algorithms for generating the A-E relationships are available in Li et al. (2020)).

5. Results and Uncertainties

5.1 Validation results

5.1.1 Comparing water surface areas with Landsat measurements

At the global scale, long-term in situ reservoir area records are still lacking. Therefore, we compared the MODIS area values with Landsat based results (at a finer spatial resolution of 30 m) for purposes of area validation. The Landsat monthly reservoir area values for all of the 164 reservoirs were collected from Global Reservoir Surface Area Dataset (GRSAD; Zhao and Gao (2018)) between 2000 and 2018. GRSAD corrected the water area underestimation of the GSWD dataset (Pekel et al. 2016) caused by both cloud contamination and the Landsat-7 scan line corrector failure (Zhao and Gao 2018). Note that the Landsat based area estimation for a given month was based on the one or two images obtained during that month, while the monthly MODIS area value was derived from the composite of the 8-day classification. However, due to the deficiency of the in-situ area values, we used this Landsat based dataset to validate the overall consistency of the MODIS area products.

According to Figure 8, the MODIS based area values agree well with the Landsat based results (with an R^2 value over 0.99). Additionally, the data points are mainly centered on the 1:1 line (slope = 0.99). The disagreements that do exist can be attributed to two sources: The first is because Landsat and MODIS collected data at different times. If a reservoir experienced a large change within a month, it may have caused a large area discrepancy. The second is related to the low spatial resolution of MODIS, which makes it more susceptible to mixed pixels. This can explain the area underestimations for relatively small reservoirs.

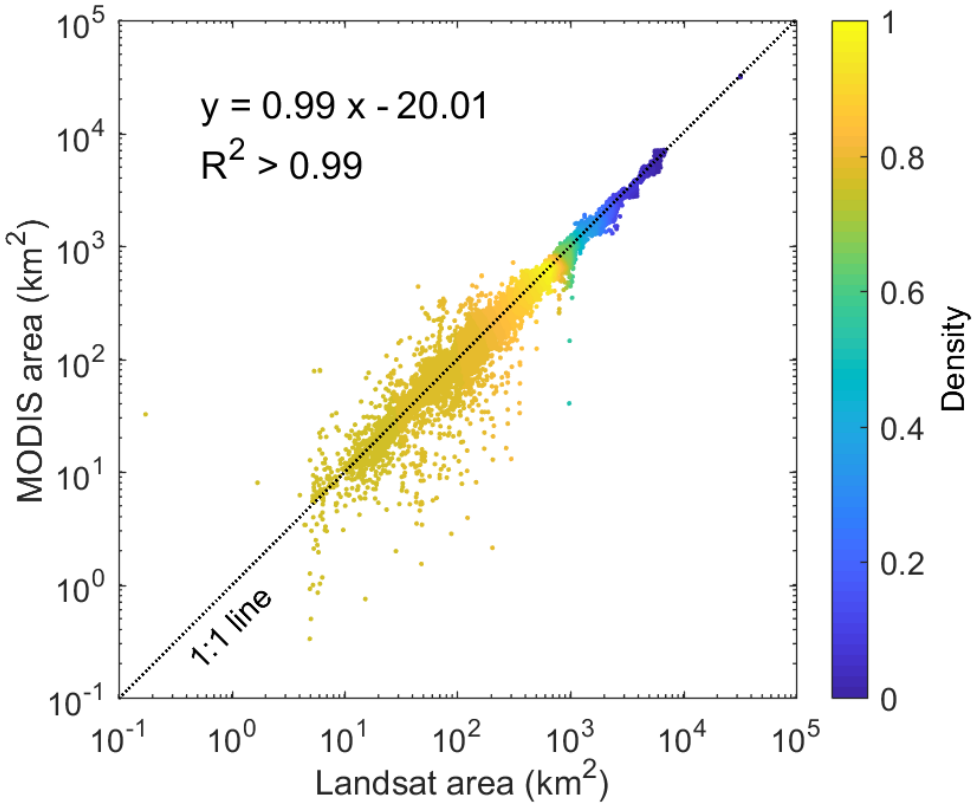

Figure 8. The density plot of monthly area estimations between Landsat and MODIS from February 2000 to December 2018 for the 164 reservoirs. Note that the x-axis and y-axis use a logarithmic scale, and there are a total of 37228 (227×164) pairs.

5.1.2. Validating the MODIS elevation and storage products against in situ observations

For the elevation and storage validations, we collected in situ daily observations for twelve Indian reservoirs (Ukai, Matatila, Rana Pratap Sagar, Gandhi Sagar, Ban Sagar, Bargi, Hirakud, Jayakwadi, Sriram Sagar, Nagarjuna Sagar, Yeleru, and Tungabhadra) from the Indian Central Water Commission (http://cwc.gov.in/) between 2000 and 2019.

The validation results of the 8-day MODIS elevation and storage products are shown in Figure 9 and Figure 10, respectively. Overall, the elevation estimations from MODIS agree well with

the in-situ data (Figure 9), with an average R^2 value of 0.87, an average RMSE value of 2.22 m, and an average NRMSE value of 12.28%. The biases (e.g., overestimation for Tungabhadra and underestimation for Yeleru) are caused by a combination of mixed pixels of reservoir edge, parameterization of the enhancement algorithm, and the mismatch of MODIS water areas with Landsat water areas, which were used to derive A-E relationships for GRBD (Li et al. 2020). With regard to the storage validations (Figure 10), they have similar patterns with those of the elevation results because they were both derived from area time series. Validations against in situ data show an average R^2 value of 0.88, an average RMSE value of 0.47 km^3, and an average NRMSE value of 13.20%.

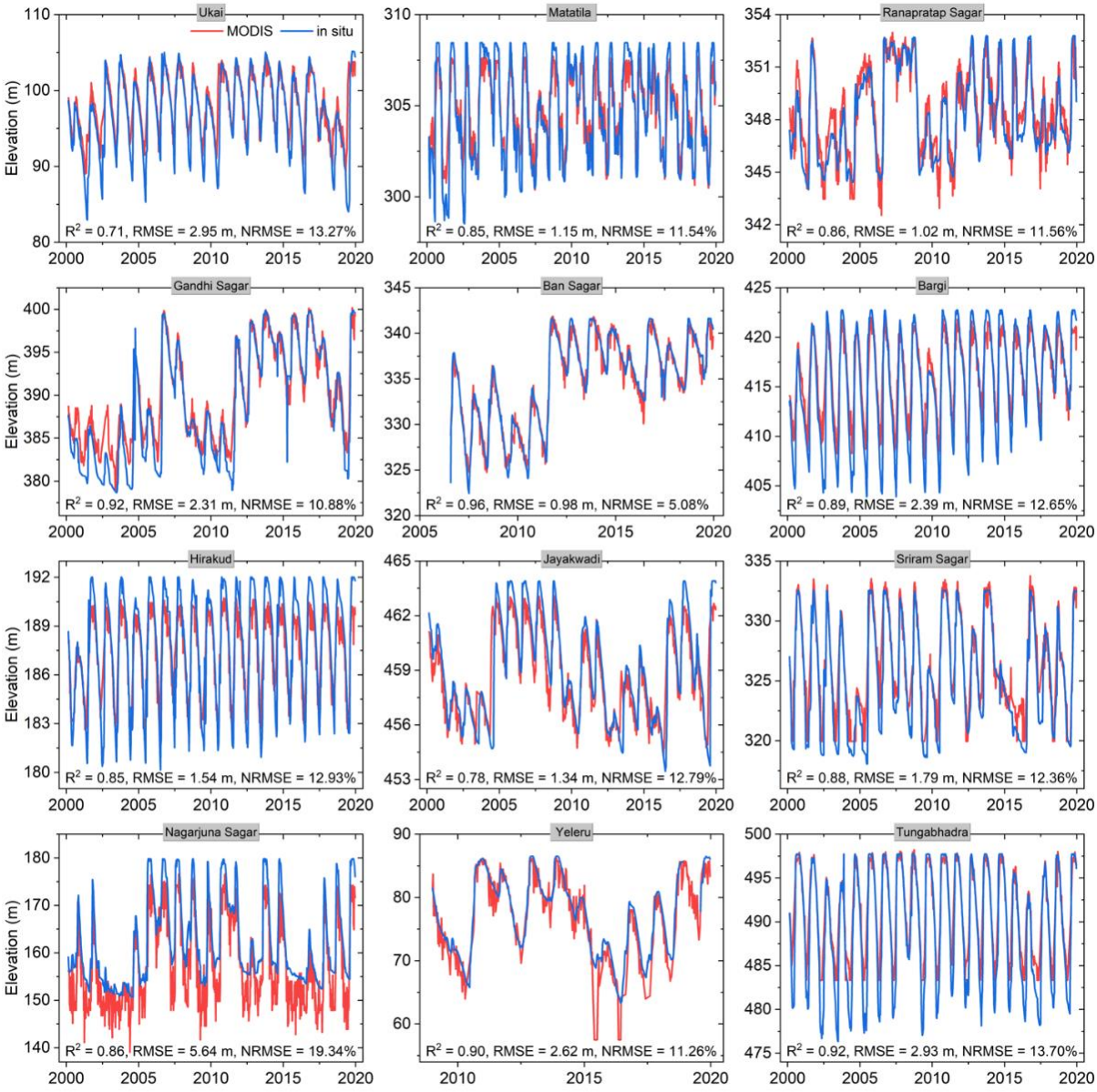

Figure 9. Validation of MODIS 8-day elevation products for twelve Indian reservoirs from 2000 to 2019.

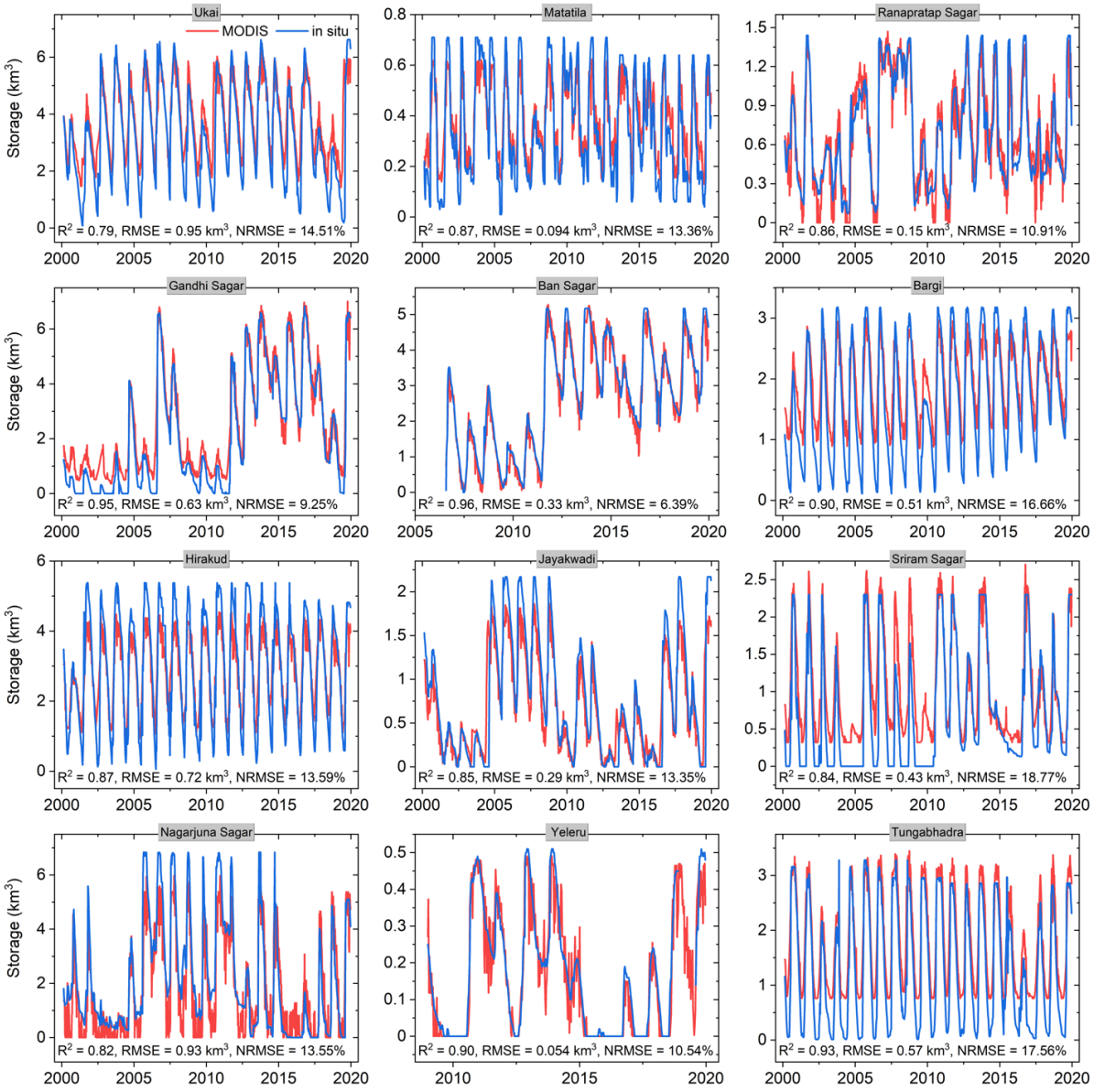

Figure 10. Validation of MODIS 8-day storage products for twelve Indian reservoirs from 2000 to 2019.

Next, we validated the monthly elevation and storage products over these twelve Indian reservoirs. The daily in situ elevation and storage values were averaged at a monthly step, which were then compared to the monthly MODIS products (Figure 11 and 12). The validation results show similar patterns as those of the 8-day products, but higher accuracies. This is because the monthly reservoir area values were generated from the composited results of three or four 8-day reservoir areas from MxD28C2, and the composition process greatly reduced the adverse effects of cloud contamination at the 8-day time step. As shown in Figure 11, the MODIS based elevations show good consistency with the in situ measured data, with an average R^2 value of 0.90, an average RMSE value of 1.99 m, and an average NRMSE value of

11.33%. Regarding the storage validations (Figure 12), the results are consistent with those of the elevations—with an average R^2 value of 0.91, an average RMSE value of 0.43 km^3, and an average NRMSE value of 11.91%.

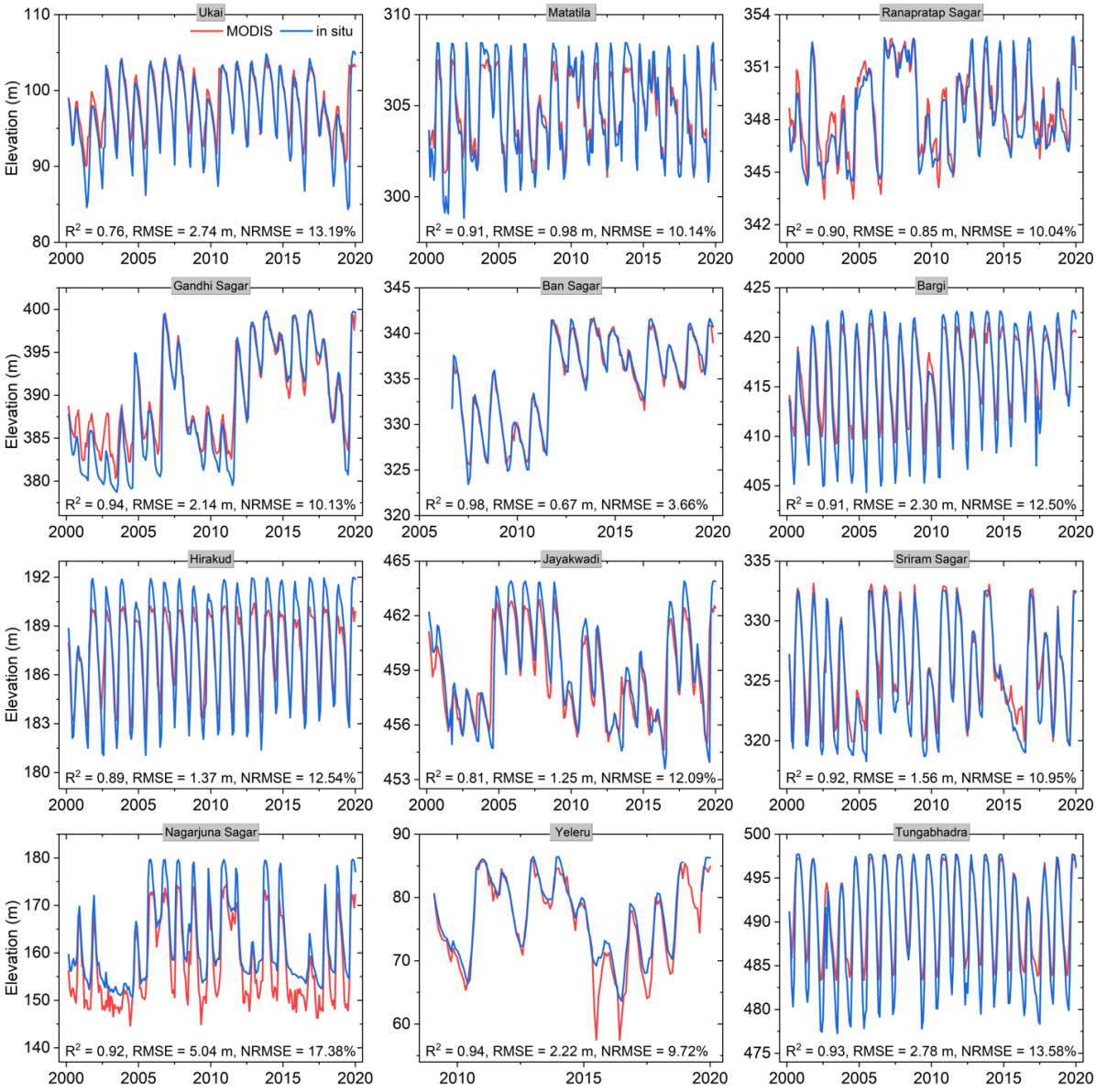

Figure 11. Validation of monthly elevation products for twelve Indian reservoirs from 2000 to 2019.

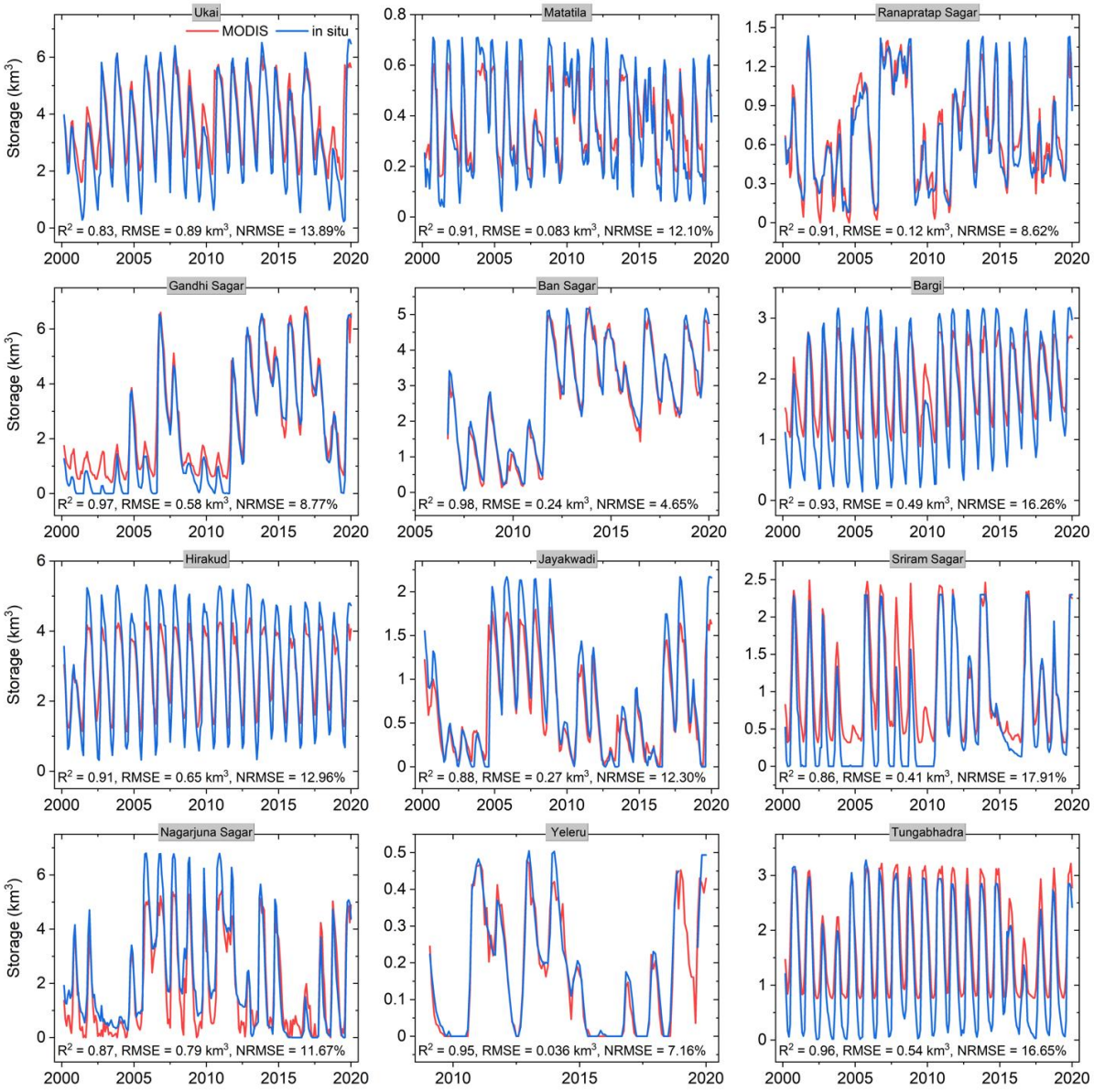

Figure 12. Validation of monthly storage products for twelve Indian reservoirs from 2000 to 2019.

5.1.3. Validating the evaporation rate product against in situ observations

The evaporation rate results were validated over two locations—Lake Nasser in Africa, and Lake Mead in North America—where in situ observations are available. The eddy covariance (EC) evaporation rate measurements for Lake Mead between 2010 and 2015 were provide by the United States Geological Survey (USGS) (Moreo 2015) With regard to Lake Nasser, the evaporation rate estimations were obtained using the Bowen ratio energy budget (BREB) method (Elsawwaf et al. 2010). Although it is not as accurate as EC observations, the BREB method has been widely utilized to estimate evaporation rates due to its operability and reliability (Lenters et al. 2005). As seen in Figure 13, the MODIS evaporation rate products

have an overall good agreement with values obtained via observation. Compared to the results which were calculated using the regular Penman equation (without heat storage), our MODIS evaporation rate estimates have shown great improvement in terms of both annual peak values and seasonal variations. For Lake Nasser, the R^2 value increases from 0.30 to 0.61, with the NRMSE decreasing from 26.86% to 16.25%. A greater improvement is observed for Lake Mead in terms of both R^2 (from 0.26 to 0.66) and NRMSE (from 41.06% to 21.76%). These results suggest that better evaporation rate estimates are achieved when considering heat storage within the algorithm.

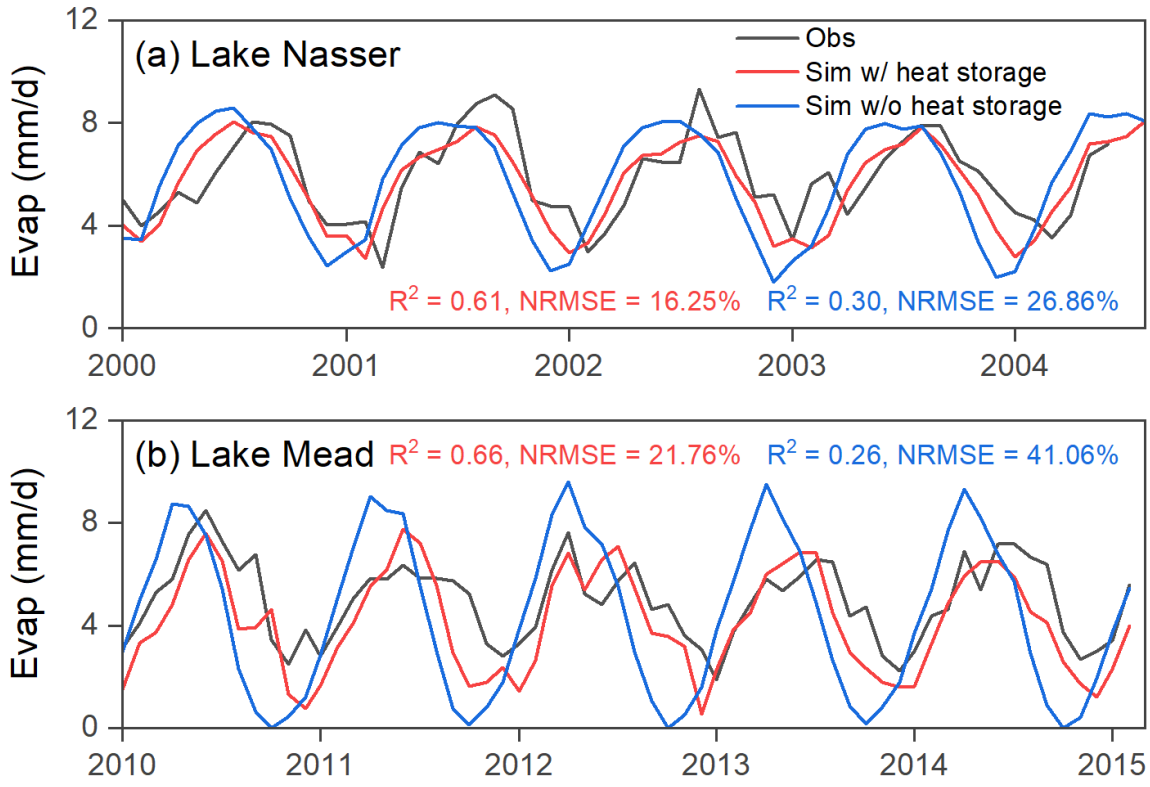

Figure 13. Validation of the evaporation rates for (a) Lake Nasser and (b) Lake Mead using Bowen ratio energy budget (BREB) estimations and eddy covariance (EC) measurements. The evaporation rate for Lake Mead (from 2010 to 2015) was calculated using MYD21A2 LST data because current version of MOD21A2 only covers the years from 2000 to 2005 (when acquired in Nov 2020). Evaporation rate for Lake Nasser (from 2000 to 2004) was calculated using MOD21A2 because the MYD21A2 product started from July 2002.

5.2 Sources of uncertainties

The sources of uncertainty with regard to the MODIS reservoir surface area are associated with both the raw image classification using the MODIS reflectance product, and the classification enhancement algorithm. The accuracy of the Ostu classification of the MODIS NIR images is affected by the mixed pixels (i.e., partially covered by water and partially covered by land) at the reservoir boundaries, as well as by ice over the lakes. The reliability of the enhancement algorithm depends on the data quality of both the water occurrence image and the raw water classification. In high latitude regions, the water occurrence image generally shows small surface area dynamics (i.e., the distribution of occurrence values highly skewed to the left). Thus, the pixels with low occurrence values have relatively large uncertainties.

The reservoir elevation and storage estimation uncertainties include reservoir surface area uncertainties (see above), A-E relationship uncertainties, and the reservoir configuration uncertainties. According to Equation (5), the estimated storage will be biased if the characteristics at capacity (storage, area, and elevation) are not accurate. Even when these factors have been correctly documented, the storage capacity may have changed due to sedimentation over time. Since the reservoir elevations are inferred only from areas and A-E relationships, they are not affected by reservoir configuration uncertainties.

Sources of evaporation rate uncertainty mainly include forcing data uncertainty and model structure/parameter uncertainty. Specifically, the forcing data used in this study (i.e. GLADS-2) is a land-based meteorological record. Although the increased humidity on the lake surface is represented by the wind function (McJannet et al. 2012; Zhao and Gao 2019), differences in the wind speeds between lake and land regions are ignored—which might introduce some uncertainties (Schwab and Morton 1984). In addition, the LTEM and its parameters can also produce uncertainties. For example, the formulation of the light attenuation coefficient (λ_PAR) is simplified using Equations 14 and 15. However, λ_PAR is affected by suspended solids, phytoplankton concentration level, and spectral distribution of solar radiation, and thus is constantly changing (Lee et al. 2005; Pinhassi et al. 2016).

The reservoir volumetric evaporation uncertainties can be attributed to evaporation rate and surface area uncertainties, which have been discussed above.

6. References

Adler, R.F., Huffman, G.J., Chang, A., Ferraro, R., Xie, P.-P., Janowiak, J., Rudolf, B., Schneider, U., Curtis, S., & Bolvin, D. (2003). The version-2 global precipitation climatology project (GPCP) monthly precipitation analysis (1979–present). *Journal of Hydrometeorology, 4*, 1147-1167

Allen, R.G., Pereira, L.S., Raes, D., & Smith, M. (1998). Crop evapotranspiration-Guidelines for computing crop water requirements-FAO Irrigation and drainage paper 56. *Fao, Rome, 300*, D05109

Althoff, D., Rodrigues, L.N., & da Silva, D.D. (2019). Evaluating evaporation methods for estimating small reservoir water surface evaporation in the Brazilian savannah. *Water, 11*, 1942

Artale, V., Iudicone, D., Santoleri, R., Rupolo, V., Marullo, S., & D'Ortenzio, F. (2002). Role of surface fluxes in ocean general circulation models using satellite sea surface temperature: Validation of and sensitivity to the forcing frequency of the Mediterranean thermohaline circulation. *Journal of Geophysical Research: Oceans, 107*, 29-21-29-24

Beaudoing, H., & Rodell, M. (2020). GLDAS Noah Land Surface Model L4 monthly 0.25 x 0.25 degree V2.1. *Greenbelt, Maryland, USA, Goddard Earth Sciences Data and Information Services Center (GES DISC)*

Bennington, V., Notaro, M., & Holman, K.D. (2014). Improving climate sensitivity of deep lakes within a regional climate model and its impact on simulated climate. *Journal of Climate, 27*, 2886-2911

Biemans, H., Haddeland, I., Kabat, P., Ludwig, F., Hutjes, R., Heinke, J., Von Bloh, W., & Gerten, D. (2011). Impact of reservoirs on river discharge and irrigation water supply during the 20th century. *Water Resources Research, 47*

Birkett, C. (1995). The contribution of TOPEX/POSEIDON to the global monitoring of climatically sensitive lakes. *Journal of Geophysical Research: Oceans, 100*, 25179-25204

Birkett, C., Reynolds, C., Beckley, B., & Doorn, B. (2011). From research to operations: the USDA global reservoir and lake monitor. *Coastal altimetry* (pp. 19-50): Springer

Bowling, L.C., & Lettenmaier, D.P. (2010). Modeling the effects of lakes and wetlands on the water balance of Arctic environments. *Journal of Hydrometeorology, 11*, 276-295

Busker, T., de Roo, A., Gelati, E., Schwatke, C., Adamovic, M., Bisselink, B., Pekel, J.F., & Cottam, A. (2019). A global lake and reservoir volume analysis using a surface water dataset and satellite altimetry. *Hydrology and Earth System Sciences, 23*, 669-690

Cooke, G.D., Welch, E.B., Peterson, S., & Nichols, S.A. (2016). *Restoration and management of lakes and reservoirs*. CRC press

Crétaux, J.-F., Jelinski, W., Calmant, S., Kouraev, A., Vuglinski, V., Bergé-Nguyen, M., Gennero, M.-C., Nino, F., Del Rio, R.A., & Cazenave, A. (2011). SOLS: A lake database to monitor in the Near Real Time water level and storage variations from remote sensing data. *Advances in space research, 47*, 1497-1507

Derber, J.C., Parrish, D.F., & Lord, S.J. (1991). The new global operational analysis system at the National Meteorological Center. *Weather and Forecasting, 6*, 538-547

Devlin, M., Barry, J., Mills, D., Gowen, R., Foden, J., Sivyer, D., & Tett, P. (2008). Relationships between suspended particulate material, light attenuation and Secchi depth in UK marine waters. *Estuarine, Coastal and Shelf Science, 79*, 429-439

Donchyts, G., Baart, F., Winsemius, H., Gorelick, N., Kwadijk, J., & Van De Giesen, N. (2016). Earth's surface water change over the past 30 years. *Nature climate change, 6*, 810

Dos Reis, R.J., & Dias, N.L.s. (1998). Multi-season lake evaporation: energy-budget estimates and CRLE model assessment with limited meteorological observations. *Journal of Hydrology, 208*, 135-147

Ellis, C.R., Stefan, H.G., & Gu, R. (1991). Water temperature dynamics and heat transfer beneath the ice cover of a lake. *Limnology and Oceanography, 36*, 324-334

Elsawwaf, M., Willems, P., Pagano, A., & Berlamont, J. (2010). Evaporation estimates from Nasser Lake, Egypt, based on three floating station data and Bowen ratio energy budget. *Theoretical and applied climatology, 100*, 439-465

Escobedo, J.F., Gomes, E.N., Oliveira, A.P., & Soares, J. (2009). Modeling hourly and daily fractions of UV, PAR and NIR to global solar radiation under various sky conditions at Botucatu, Brazil. *Applied Energy, 86*, 299-309

Fairall, C., Bradley, E.F., Godfrey, J., Wick, G., Edson, J.B., & Young, G. (1996). Cool-skin and warm-layer effects on sea surface temperature. *Journal of Geophysical Research: Oceans, 101*, 1295-1308

Fang, X., & Stefan, H.G. (1996). Long-term lake water temperature and ice cover simulations/measurements. *Cold Regions Science and Technology, 24*, 289-304

Friedrich, K., Grossman, R.L., Huntington, J., Blanken, P.D., Lenters, J., Holman, K.D., Gochis, D., Livneh, B., Prairie, J., & Skeie, E. (2018). Reservoir evaporation in the Western United States: current science, challenges, and future needs. *Bulletin of the American Meteorological Society, 99*, 167-187

Gao, H., Birkett, C., & Lettenmaier, D.P. (2012). Global monitoring of large reservoir storage from satellite remote sensing. *Water Resources Research, 48*

Gianniou, S.K., & Antonopoulos, V.Z. (2007). Evaporation and energy budget in Lake Vegoritis, Greece. *Journal of Hydrology, 345*, 212-223

Håkanson, L. (1995). Models to predict Secchi depth in small glacial lakes. *Aquatic Sciences, 57*, 31-53

Haklay, M., & Weber, P. (2008). Openstreetmap: User-generated street maps. *IEEE Pervasive Computing, 7*, 12-18

Hostetler, S.W., & Bartlein, P.J. (1990). Simulation of lake evaporation with application to modeling lake level variations of Harney-Malheur Lake, Oregon. *Water Resources Research, 26*, 2603-2612

Hulley, G., & Hook, S. (2017). MOD21 MODIS/Terra Land Surface Temperature/3-Band Emissivity 5-Min L2 1km V006 [Data set]. *NASA EOSDIS Land Processes DAAC*

Kalnay, E., Kanamitsu, M., Kistler, R., Collins, W., Deaven, D., Gandin, L., Iredell, M., Saha, S., White, G., & Woollen, J. (1996). The NCEP/NCAR 40-year reanalysis project. *Bulletin of the American Meteorological Society, 77*, 437-472

Khandelwal, A., Karpatne, A., Marlier, M.E., Kim, J., Lettenmaier, D.P., & Kumar, V. (2017). An approach for global monitoring of surface water extent variations in reservoirs using MODIS data. *Remote Sensing of Environment, 202*, 113-128

Lee, Z.P., Darecki, M., Carder, K.L., Davis, C.O., Stramski, D., & Rhea, W.J. (2005). Diffuse attenuation coefficient of downwelling irradiance: An evaluation of remote sensing methods. *Journal of Geophysical Research: Oceans, 110*

Lenters, J.D., Kratz, T.K., & Bowser, C.J. (2005). Effects of climate variability on lake evaporation: Results from a long-term energy budget study of Sparkling Lake, northern Wisconsin (USA). *Journal of Hydrology, 308*, 168-195

Li, Y., Gao, H., Zhao, G., & Tseng, K.-H. (2020). A high-resolution bathymetry dataset for global reservoirs using multi-source satellite imagery and altimetry. *Remote Sensing of Environment, 244*, 111831

Ling, F., Li, X., Foody, G.M., Boyd, D., Ge, Y., Li, X., & Du, Y. (2020). Monitoring surface water area variations of reservoirs using daily MODIS images by exploring sub-pixel information. *Isprs Journal of Photogrammetry and Remote Sensing, 168*, 141-152

McFeeters, S.K. (1996). The use of the Normalized Difference Water Index (NDWI) in the delineation of open water features. *International Journal of Remote Sensing, 17*, 1425-1432

McJannet, D., Webster, I., Stenson, M., & Sherman, B. (2008). *Estimating open water evaporation for the Murray-Darling basin: A report to the Australian government from the CSIRO Murray-Darling basin sustainable yields project*. CSIRO Canberra, Australia

McJannet, D.L., Webster, I.T., & Cook, F.J. (2012). An area-dependent wind function for estimating open water evaporation using land-based meteorological data. *Environmental modelling & software, 31*, 76-83

McMahon, T., Peel, M., Lowe, L., Srikanthan, R., & McVicar, T. (2013). Estimating actual, potential, reference crop and pan evaporation using standard meteorological data: a pragmatic synthesis. *Hydrol. Earth Syst. Sci, 17*, 1331-1363

Mehran, A., Mazdiyasni, O., & AghaKouchak, A. (2015). A hybrid framework for assessing socioeconomic drought: Linking climate variability, local resilience, and demand. *Journal of Geophysical Research: Atmospheres, 120*, 7520-7533

Meng, X., Liu, H., Du, Q., Xu, L., & Liu, Y. (2020). Evaluation of the Performance of Different Methods for Estimating Evaporation over a Highland Open Freshwater Lake in Mountainous Area. *Water, 12*, 3491

Messager, M.L., Lehner, B., Grill, G., Nedeva, I., & Schmitt, O. (2016). Estimating the volume and age of water stored in global lakes using a geo-statistical approach. *Nature communications, 7*, 1-11

Mhawej, M., Fadel, A., & Faour, G. (2020). Evaporation rates in a vital lake: a 34-year assessment for the Karaoun Lake. *International Journal of Remote Sensing, 41*, 5321-5337

Moreo, M. (2015). Evaporation data from Lake Mead and Lake Mohave, Nevada and Arizona, March 2010 through April 2015. *US Geological Survey*,

Mu, Q., Zhao, M., & Running, S.W. (2011). Improvements to a MODIS global terrestrial evapotranspiration algorithm. *Remote Sensing of Environment, 115*, 1781-1800

Murdock, H.E., Gibb, D., André, T., Appavou, F., Brown, A., Epp, B., Kondev, B., McCrone, A., Musolino, E., & Ranalder, L. (2019). Renewables 2019 Global Status Report

Otsu, N. (1979). A threshold selection method from gray-level histograms. *IEEE transactions on systems, man, and cybernetics, 9*, 62-66

Pekel, J.-F., Cottam, A., Gorelick, N., & Belward, A.S. (2016). High-resolution mapping of global surface water and its long-term changes. *Nature, 540*, 418-422

Pinhassi, J., DeLong, E.F., Béjà, O., González, J.M., & Pedrós-Alió, C. (2016). Marine bacterial and archaeal ion-pumping rhodopsins: genetic diversity, physiology, and ecology. *Microbiology and Molecular Biology Reviews, 80*, 929-954

Plate, E.J. (2002). Flood risk and flood management. *Journal of Hydrology, 267*, 2-11

Rodell, M., Houser, P., Jambor, U., Gottschalck, J., Mitchell, K., Meng, C.-J., Arsenault, K., Cosgrove, B., Radakovich, J., & Bosilovich, M. (2004). The global land data assimilation system. *Bulletin of the American Meteorological Society, 85*, 381-394

Schewe, J., Heinke, J., Gerten, D., Haddeland, I., Arnell, N.W., Clark, D.B., Dankers, R., Eisner, S., Fekete, B.M., & Colón-González, F.J. (2014). Multimodel assessment of water scarcity under climate change. *Proceedings of the National Academy of Sciences, 111*, 3245-3250

Schwab, D.J., & Morton, J.A. (1984). Estimation of overlake wind speed from overland wind speed: A comparison of three methods. *Journal of Great Lakes Research, 10*, 68-72

Schwatke, C., Dettmering, D., Bosch, W., & Seitz, F. (2015). DAHITI–an innovative approach for estimating water level time series over inland waters using multi-mission satellite altimetry. *Hydrology and Earth System Sciences, 19*, 4345-4364

Subin, Z.M., Riley, W.J., & Mironov, D. (2012). An improved lake model for climate simulations: Model structure, evaluation, and sensitivity analyses in CESM1. *Journal of Advances in Modeling Earth Systems, 4*

Tanny, J., Cohen, S., Assouline, S., Lange, F., Grava, A., Berger, D., Teltch, B., & Parlange, M. (2008). Evaporation from a small water reservoir: Direct measurements and estimates. *Journal of Hydrology, 351*, 218-229

Tu, C.Y., & Tsuang, B.J. (2005). Cool-skin simulation by a one-column ocean model. *Geophysical Research Letters, 32*

Veldkamp, T., Wada, Y., Aerts, J., Döll, P., Gosling, S.N., Liu, J., Masaki, Y., Oki, T., Ostberg, S., & Pokhrel, Y. (2017). Water scarcity hotspots travel downstream due to human interventions in the 20th and 21st century. *Nature communications, 8*, 15697

Vermote, E. (2015). MOD09Q1 MODIS/Terra Surface Reflectance 8-Day L3 Global 250m SIN Grid V006 [Data set]. *NASA EOSDIS Land Processes DAAC*

Vickers, D., Mahrt, L., & Andreas, E.L. (2015). Formulation of the sea surface friction velocity in terms of the mean wind and bulk stability. *Journal of Applied Meteorology and Climatology, 54*, 691-703

Weisman, R.N., & Brutsaert, W. (1973). Evaporation and cooling of a lake under unstable atmospheric conditions. *Water Resources Research, 9*, 1242-1257

Winter, T.C., Rosenberry, D.O., & Sturrock, A. (1995). Evaluation of 11 equations for determining evaporation for a small lake in the north central United States. *Water Resources Research, 31*, 983-993

Yao, F., Wang, J., Wang, C., & Crétaux, J.-F. (2019). Constructing long-term high-frequency time series of global lake and reservoir areas using Landsat imagery. *Remote Sensing of Environment, 232*, 111210

Yigzaw, W., Li, H.Y., Demissie, Y., Hejazi, M.I., Leung, L.R., Voisin, N., & Payn, R. (2018). A New Global Storage-Area-Depth Dataset for Modeling Reservoirs in Land Surface and Earth System Models. *Water Resources Research, 54*, 10,372-310,386

Zhang, H., Gorelick, S.M., Zimba, P.V., & Zhang, X. (2017). A remote sensing method for estimating regional reservoir area and evaporative loss. *Journal of Hydrology, 555*, 213-227

Zhang, S., Gao, H., & Naz, B.S. (2014). Monitoring reservoir storage in South Asia from multisatellite remote sensing. *Water Resources Research, 50*, 8927-8943

Zhao, G., & Gao, H. (2018). Automatic correction of contaminated images for assessment of reservoir surface area dynamics. *Geophysical Research Letters, 45*, 6092-6099

Zhao, G., & Gao, H. (2019). Estimating reservoir evaporation losses for the United States: Fusing remote sensing and modeling approaches. *Remote Sensing of Environment, 226*, 109-124

Zhao, G., Gao, H., & Cai, X. (2020). Estimating lake temperature profile and evaporation losses by leveraging MODIS LST data. *Remote Sensing of Environment, 251*, 112104

Zhou, T., Nijssen, B., Gao, H., & Lettenmaier, D.P. (2016). The contribution of reservoirs to global land surface water storage variations. *Journal of Hydrometeorology, 17*, 309-325

Zhou, Y. (2020). Exploring multidecadal changes in climate and reservoir storage for assessing nonstationarity in flood peaks and risks worldwide by an integrated frequency analysis approach. *Water Research, 185*, 116265

Appendix-A

Table A1. List of the 164 reservoirs and their attributes

ID	GRanD_id	Res_name	Country	Continent	A-E Coeff.[1] *a, b*	Vc (km^3)	Ac (km^2)	Ec (m)	Average Depth (m)	Lon (◦)	Lat (◦)
1*	5058	Baikal	Russia	Asia	0.0045,312.77	23,615.4	32265.61	456.88	738.70	104.32	52.24
2	3667	Volta	Ghana	Africa	0.0037,55.59	148.0	8502.00	86.65	24.50	0.06	6.30
3	4478	Nasser	Egypt	Africa	0.0047,152.82	162.0	6500.00	183.28	30.10	32.89	23.97
4	4056	Kariba Reservoir	Zambia	Africa	0.011,424.98	180.0	5400.00	485.41	35.10	28.76	-16.52
5	5055	Bratsk Reservoir	Russia	Asia	0.0066,367.92	169.3	5470.00	403.85	35.10	101.78	56.29
6	4787	Zaysan	Kazakhstan	Asia	0.0047,370.21	49.8	5490.00	395.74	12.60	83.35	49.66
7	2294	Guri Reservoir	Venezuela	South America	0.014,217.17	135.0	4250.00	278.38	36.90	-63.00	7.77
8	1995	Caniapiscau Reservoir	Canada	North America	0.012,489	53.8	4275.00	541.08	15.20	-69.78	54.85
9	1394	Robert Bourassa Reservoir	Canada	North America	0.011,143.99	61.7	2905.00	176.24	22.40	-77.45	53.79
10	2516	Sobradinho Reservoir	Brazil	South America	0.0057,375.27	34.1	3017.90	392.50	13.00	-40.82	-9.42
11	712	Cedar	Canada	North America	0.0022,250.49	9.6	2668.46	256.29	3.90	-99.29	53.16
12	1396	La Grande 3 Reservoir	Canada	North America	0.025,195.26	60.0	2451.00	257.48	25.00	-75.96	53.73
13	2365	Tucurui Reservoir	Brazil	South America	0.013,40.96	45.5	2606.00	75.40	21.10	-49.65	-3.83
14	4375	Tsimlyanskoye Reservoir	Russia	Euro	0.012,7.64	23.9	2702.00	39.44	10.60	42.11	47.61
15	5834	Zeyskoye Reservoir	Russia	Asia	0.021,266.44	68.4	2420.00	316.41	30.60	127.31	53.77

16	5180	Vilyuy Reservoir	Russia	Asia	0.029,182.74	35.9	2170.00	244.62	16.40	112.48	63.03
17	4783	Khantayskoye Reservoir	Russia	Asia	0.0044,49.76	23.5	2221.61	59.64	10.70	87.81	68.16
18	4505	Cahora Bassa Reservoir	Mozambique	Africa	0.015,286.96	55.8	2739.00	329.18	30.80	32.70	-15.58
19	6	Williston	Canada	North America	0.053,580.99	39.5	1773.00	674.79	43.20	-122.20	56.02
20	4472	Buhayrat ath Tharthar	Iraq	Asia	0.04,-19.46	85.6	2135.54	65.00	25.60	43.46	33.69
21	5056	Krasnoyarsk Reservoir	Russia	Asia	0.039,162.77	73.3	2000.00	240.04	45.00	92.29	55.93
22	4623	Kama Reservoir	Russia	Euro	0.0074,96.08	12.2	1915.00	110.32	7.70	56.34	58.12
23	1957	Okeechobee	United States of America	North America	0.0062,-5.57	5.2	1536.80	3.90	4.00	-81.10	26.94
24	5295	Hungtze	China	Asia	0.0075,1.46	13.5	2074.61	17.00	9.80	118.73	33.09
25	4474	Razazah	Iraq	Asia	0.015,11.07	25.8	1621.00	34.69	19.50	43.89	32.70
26	2023	Gouin Reservoir	Canada	North America	0.00068,402.91	8.6	1570.00	403.98	6.50	-74.10	48.36
27	4789	Qapshaghay Bogeni Reservoir	Kazakhstan	Asia	0.009,467.11	28.1	1850.00	483.71	23.30	77.10	43.92
28	753	Fort Berthold Reservoir	United States of America	North America	0.025,528.65	29.4	1477.40	565.10	26.80	-101.43	47.51
29	2445	Aperea Reservoir	Paraguay	South America	0.022,48.84	21.0	1600.00	84.71	18.90	-56.63	-27.39
30	870	Oahe	United States of America	North America	0.022,462.73	28.3	1429.57	493.78	26.60	-100.40	44.46
31	2390	Ilha Solteira Reservoir	Brazil	South America	0.032,290.95	21.2	1200.00	329.78	19.70	-51.38	-20.37
32	4629	Saratov Reservoir	Russia	Euro	0.026,-0.28	12.9	1117.70	28.36	12.00	47.76	52.05
33	4350	Imandra	Russia	Euro	0.19,-62.87	10.8	1062.37	136.07	10.20	32.55	67.41

34	3640	Kainji Reservoir	Nigeria	Africa	0.04,94	15.0	1071.23	136.81	14.50	4.61	9.87
35	4785	Novosibirskoye	Russia	Asia	0.014,98.78	8.8	1070.00	113.97	8.60	83.00	54.84
36	4625	Cheboksary	Russia	Euro	0.024,39.3	13.9	1080.38	65.73	12.70	47.46	56.14
37	4359	Ilmen	Russia	Euro	0.0083,9.98	12.0	1120.00	19.28	12.50	31.28	58.46
38	4480	Jebel Aulia Reservoir	Sudan	Africa	0.0062,375.01	3.5	861.19	380.39	3.70	32.48	15.24
39	1397	Opinaca Reservoir	Canada	North America	0.021,194.08	8.5	1040.00	216.10	9.10	-76.58	52.21
40	2392	Furnas	Brazil	South America	0.044,720.07	22.6	1127.07	769.32	24.70	-46.31	-20.67
41	2368	Serra da Mesa Reservoir	Brazil	South America	0.034,410.2	54.4	1784.00	470.07	59.00	-48.30	-13.84
42	4624	Votkinsk Reservoir	Russia	Euro	0.039,53.14	9.4	850.82	86.25	11.20	54.08	56.80
43	6201	Argyle Reservoir	Australia	Oceania	0.028,66.44	10.8	981.21	93.97	13.00	128.74	-16.12
44	731	Rainy	Canada	North America	0.00078,336.09	0.7	829.45	336.73	8.00	-93.36	48.62
45	307	Fort Peck	United States of America	North America	0.044,643.32	22.8	969.86	685.76	28.90	-106.41	48.00
46	2375	Tres Marias Reservoir	Brazil	South America	0.036,539.11	21.0	1040.00	576.06	26.30	-45.27	-18.21
47	2012	Pipmuacan Reservoir	Canada	North America	0.05,360.46	13.9	978.00	409.16	17.60	-69.77	49.36
48	4679	Chardarinskoye	Kazakhstan	Asia	0.018,238.24	5.7	800.66	252.54	9.00	67.96	41.25
49	4626	Nizhnekamsk Reservoir	Russia	Euro	0.014,50.37	13.8	1084.00	65.34	18.70	52.28	55.70
50	2456	Negro Reservoir	Uruguay	South America	0.019,62.01	8.8	1070.00	82.77	12.20	-56.42	-32.83
51	2343	Chocon Reservoir	Argentina	South America	0.015,365.75	22.0	820.00	378.20	30.90	-68.76	-39.27
52	4442	Ataturk Dam	Turkey	Asia	0.11,454.25	48.7	817.00	541.20	70.10	38.32	37.49

53	2513	Itaparica Reservoir	Brazil	South America	0.033,279.33	10.7	781.21	305.40	15.70	-38.31	-9.14
54	4464	Assad	Syria	Asia	0.059,266.63	11.7	610.00	302.87	18.20	38.55	35.86
55	3650	Lagdo Reservoir	Cameroon	Africa	0.037,190.16	7.7	691.12	216.00	12.50	13.69	9.06
56	1269	Toledo Bend Reservoir	United States of America	North America	0.02,39.46	5.5	636.18	52.43	10.50	-93.57	31.18
57	6922	Eastmain Reservoir	Canada	North America	0.068,245.92	6.9	602.90	286.82	11.51	-75.89	52.19
58	2009	Outardes 4 Reservoir	Canada	North America	0.19,239.61	24.5	640.00	361.53	41.50	-68.91	49.71
59	4349	Kovdozero	Russia	Euro	0.0019,78.18	3.7	745.00	79.62	19.70	31.76	68.60
60	2380	Sao Simao Reservoir	Brazil	South America	0.052,369.17	12.5	703.00	405.94	21.50	-50.50	-19.02
61	610	Mead	United States of America	North America	0.14,288.76	34.1	659.30	374.60	63.20	-114.73	36.02
62	5087	Yamdrok	China	Asia	0.013,4435.36	14.6	638.00	4443.49	28.20	90.38	29.10
63	1391	Angostura Reservoir	Mexico	North America	0.081,478.96	18.2	640.00	530.67	16.20	-92.78	16.40
64	4991	Srisailam Reservoir	India	Asia	0.031,253.3	8.3	534.05	269.75	16.30	78.90	16.09
65	2455	Grande Reservoir	Argentina	South America	0.031,16.89	5.0	592.83	35.08	10.30	-57.94	-31.27
66	4843	Gandhisagar Reservoir	India	Asia	0.034,379.03	6.8	619.89	399.90	14.00	75.55	24.70
67	2397	Promissao Reservoir	Brazil	South America	0.08,342.73	7.4	513.39	384.00	14.50	-49.78	-21.30
68	282	Arrow	Canada	North America	0.17,351.07	10.3	504.82	439.30	22.20	-117.78	49.34
69	2382	Agua Vermelha Reservoir	Brazil	South America	0.056,351.62	11.0	563.15	383.30	21.90	-50.35	-19.87

70	4898	Hirakud Reservoir	India	Asia	0.022,177.26	5.4	669.62	192.02	16.20	83.85	21.52
71	3041	Kossour Reservoir	Ivory Coast	Africa	0.034,169.78	27.7	1058.20	206.00	55.30	-5.47	7.03
72	4784	Kureiskaya	Russia	Asia	0.05,67.89	10.0	558.00	95.63	19.80	88.29	66.95
73	3071	Storsjon	Sweden	Euro	0.0042,291.09	8.0	484.60	293.13	38.30	14.47	63.30
74	316	Flathead Lake	United States of America	North America	0.13,816.09	23.2	510.00	883.61	50.20	-114.23	47.68
75	2004	Kempt	Canada	North America	0.033,478.6	2.2	470.44	494.18	4.70	-70.53	50.66
76	6700	Kolyma dam	Russia	Asia	0.14,390.91	15.1	454.60	453.00	33.17	150.23	62.05
77	4501	Mtera Reservoir	United Republic of Tanzania	Africa	0.022,688.05	3.2	478.83	698.50	7.20	35.98	-7.14
78	4686	Kayrakkumskoye	Tajikistan	Asia	0.021,335.24	4.2	513.00	346.23	9.70	69.82	40.28
79	250	Kinbasket	Canada	North America	0.32,622.77	24.8	430.00	759.15	59.60	-118.57	52.08
80	4634	Mingechaurskoye	Azerbaijan	Asia	0.072,42.02	15.7	567.97	83.00	38.50	47.03	40.80
81	2431	Lago del Río Yguazú	Paraguay	South America	0.045,203.13	8.5	620.00	231.14	20.80	-54.97	-25.37
82	4858	Govind Ballabah Pant	India	Asia	0.062,241.75	5.7	426.36	268.22	26.60	83.00	24.20
83	4422	Keban Baraji	Turkey	Asia	0.11,772.51	30.6	675.00	848.79	77.00	38.76	38.81
84	2340	Los Barreales	Argentina	South America	0.31,290.07	27.7	413.00	417.11	67.07	-68.69	-38.58
85	4859	Bansagar Lake	India	Asia	0.051,317.64	5.2	471.60	341.64	14.10	81.29	24.19
86	1275	Sam Rayburn Reservoir	United States of America	North America	0.036,35.66	3.5	455.64	50.11	20.60	-94.11	31.07
87	2414	Barra Bonita	Brazil	South America	0.0023,565.25	7.0	542.00	566.48	18.80	-49.23	-23.21
88	4739	Ukal	India	Asia	0.042,83.6	6.6	509.85	105.16	23.00	73.60	21.26

89	479	Utah Lake	United States of America	North America	0.023,1359.51	1.1	380.00	1368.28	4.70	-111.89	40.36
90	305	Pend Oreille Lake	United States of America	North America	0.23,541.66	54.2	381.47	628.80	142.08	-117.00	48.18
91	4994	Tungabhadra	India	Asia	0.041,483.34	3.3	349.42	497.74	10.70	76.33	15.27
92	4461	Mosul Dam Lake	Iraq	Asia	0.16,273.38	11.1	353.16	330.00	36.00	42.83	36.63
93	4470	Habbaniyah	Iraq	Asia	0.071,114.62	8.2	418.40	144.43	32.40	42.35	34.21
94	4946	Sriramsagar Reservoir	India	Asia	0.04,319.95	2.3	314.38	332.54	9.40	78.34	18.97
95	2376	Lago das Brisas	Brazil	South America	0.088,471.03	17.0	559.60	520.38	51.00	-49.10	-18.41
96	2356	Meelpaeg	Canada	North America	0.0041,269.36	2.2	314.90	270.65	15.00	-56.78	48.17
97	4260	Hendrik Verwoerd	South Africa	Africa	0.069,1236.1	5.3	374.00	1261.93	19.30	25.50	-30.62
98	1387	Malpaso	Mexico	North America	0.3,89.06	9.2	309.45	182.00	28.40	-93.60	17.18
99	1379	Inhernillo	Mexico	North America	0.14,116.66	12.0	400.00	173.13	32.40	-101.89	18.27
100	4184	Vaaldam	South Africa	Africa	0.036,1472.82	2.6	320.00	1484.27	11.10	28.12	-26.88
101	5062	Longyangxia	China	Asia	0.18,2518.98	24.7	383.00	2589.15	97.10	100.92	36.12
102	3727	Hoytiainen	Finland	Euro	0.0064,86.17	2.4	293.00	88.05	28.90	29.48	62.83
103	1423	Baskatong	Canada	North America	0.057,207.29	2.6	280.00	223.14	10.80	-75.98	46.72
104	5803	Tri An Lake	Vietnam	Asia	0.072,39.48	2.8	323.00	62.79	10.00	107.04	11.11
105	2007	Peribonka	Canada	North America	0.11,411.54	5.2	270.72	440.26	18.70	-71.25	49.90
106	4942	Jayakwadi	India	Asia	0.032,451.67	2.2	382.39	463.91	10.60	75.37	19.49
107	3638	Shiroro	Nigeria	Africa	0.086,350.9	7.0	312.00	377.73	25.80	6.84	9.97
108	4379	Tshchikskoye	Russia	Euro	0.062,16.04	3.0	286.28	33.68	11.30	39.12	44.99

109	710	Tobin	Canada	North America	0.009,311.23	2.2	263.86	313.59	8.40	-103.40	53.66
110	5796	Noi	Thailand	Asia	0.057,129.5	2.0	288.00	145.94	8.30	105.43	15.21
111	4483	Roseires Reservoir	Sudan	Africa	0.025,475.84	7.4	450.00	487.12	13.30	34.39	11.80
112	4675	Toktogul'skoye	Kyrgyzstan	Asia	0.55,743.53	19.5	284.30	901.24	87.30	72.65	41.68
113	6698	Gordon	Australia	Oceania	0.37,208.54	12.4	278.00	311.42	56.30	145.98	-42.73
114	4964	Ujani	India	Asia	0.055,482.17	1.5	268.91	496.83	14.30	75.12	18.07
115	2312	Hondo	Argentina	South America	0.029,266.72	1.7	330.00	276.36	8.00	-64.89	-27.52
116	4362	Ivankovo Reservoir	Russia	Euro	0.018,119.51	1.2	220.57	123.47	5.40	37.12	56.73
117	4702	Tarbela	Pakistan	Asia	0.53,351.46	13.7	250.00	483.55	66.90	72.69	34.09
118	4985	Nagarjuna	India	Asia	0.29,100.78	6.8	272.18	179.83	59.20	79.31	16.57
119	3070	Kallsjon	Sweden	Euro	0.028,387.52	6.1	189.74	392.80	39.00	13.34	63.43
120	4431	Karakaya	Turkey	Asia	0.22,631.76	9.5	298.00	697.54	49.20	39.14	38.23
121	4792	Beas	India	Asia	0.2,371.49	6.2	254.85	423.67	45.20	75.95	31.97
122	4047	Tshangalele	Democratic Republic of the Congo	Africa	0.031,1119.03	1.1	225.65	1126.03	7.10	27.24	-10.75
123	4485	Finchaa	Ethiopia	Africa	0.019,2216.55	0.7	196.13	2220.26	3.60	37.36	9.56
124	4989	Almatti	India	Asia	0.053,504.12	3.1	293.42	519.60	36.20	75.89	16.33
125	4707	Mangla	Pakistan	Asia	0.2,320.13	9.1	251.00	370.60	41.70	73.64	33.15
126	4836	Rana Pratap	India	Asia	0.14,324.74	1.4	197.66	352.81	16.90	75.58	24.92
127	3014	Bagre	Burkina Faso	Africa	0.057,223.54	1.7	255.00	238.12	10.10	-0.55	11.47
128	1991	Junin	Peru	South America	0.023,4079.84	1.1	206.71	4084.62	3.40	-76.19	-10.98
129	4881	Bargi Dam Reservoir	India	Asia	0.085,401.51	3.2	236.24	422.76	25.60	79.93	22.95
130	6686	Great Lake	Australia	Oceania	0.4,969.53	3.4	176.00	1040.54	22.60	146.73	-41.98
131	6800	Hawea	New Zealand	Oceania	0.15,323.54	2.2	150.00	345.49	100.50	169.25	-44.61

132	3676	Albufeira da Quiminha	Angola	Africa	0.13,34.99	1.6	129.05	51.93	12.70	13.79	-8.96
133	6629	Eucumbene	Australia	Oceania	0.46,1097.65	4.8	145.42	1165.24	39.50	148.62	-36.13
134	1320	Falcon Reservoir	United States of America	North America	0.07,71.74	3.9	311.84	93.48	32.50	-99.17	26.56
135	597	Lake Powell	United States of America	North America	0.14,1047.2	30.0	609.38	1127.76	40.00	-111.49	36.94
136	4463	Dukan	Iraq	Asia	0.19,462.68	7.0	270.00	513.69	56.50	44.96	35.96
137	1230	Cedar Creek Reservoir	United States of America	North America	0.094,85.92	0.8	133.03	98.15	11.30	-96.07	32.18
138	4041	Lake Maga	Cameroon	Africa	0.019,309.63	0.7	148.72	312.50	4.57	15.05	10.83
139	5157	Pasak Chonlasit	Thailand	Asia	0.053,33.59	0.8	158.87	42.00	51.50	101.08	14.85
140	6594	Fairbairn	Australia	Oceania	0.13,186.48	2.3	179.43	209.81	12.60	148.06	-23.65
141	6628	Hume	Australia	Oceania	0.15,161.82	3.0	201.90	192.00	27.40	147.03	-36.11
142	4500	Kikuletwa	United Republic of Tanzania	Africa	0.1,677.01	0.6	126.33	689.65	10.30	37.47	-3.82
143	4958	Nizam sagar	India	Asia	0.089,419.96	0.5	92.75	428.24	10.10	77.93	18.20
144	6606	Victoria	Australia	Oceania	0.17,7.53	0.7	122.00	27.73	6.30	141.28	-34.04
145	1869	Grenada Lake	United States of America	North America	0.13,49.35	1.5	128.29	65.53	31.20	-89.77	33.82
146	138	Canyon	United States of America	North America	0.69,1300.94	1.6	108.39	1373.12	15.70	-121.09	40.18
147	4638	Aras Dam Lake	Azerbaijan	Asia	0.12,762.77	1.4	145.00	779.94	13.40	45.40	39.09
148	4481	Khashm el-Girba	Sudan	Africa	0.093,463.08	1.3	125.00	474.76	13.00	35.90	14.93
149	370	Lake Cascade	United States of America	North America	0.16,1455.02	0.9	101.98	1471.57	8.50	-116.05	44.52
150	3695	Seitevare	Sweden	Euro	0.63,419.19	1.7	81.00	470.15	18.20	18.57	66.97
151	4484	Yardi	Ethiopia	Africa	0.33,533.59	2.3	104.87	568.25	26.60	40.54	10.23
152	119	Clear Lake Reservoir	United States of America	North America	0.2,1345.8	0.7	100.36	1365.84	8.10	-121.08	41.93

153	5196	Guanting Shuiku	China	Asia	0.11,465.09	4.2	130.00	479.09	25.20	115.60	40.23
154	2953	Barrage Al Massira	Morocco	Africa	0.34,241.41	2.8	80.00	268.54	31.90	-7.64	32.47
155	1319	Venustiano Carranza	Mexico	North America	0.095,252.29	1.3	150.56	266.53	16.60	-100.62	27.51
156	4471	Lake Hamrin	Iraq	Asia	0.12,80.23	4.6	228.00	107.50	7.90	44.97	34.12
157	4826	Matatila	India	Asia	0.1,297.22	0.7	112.07	308.46	17.30	78.37	25.10
158	1263	Twin Buttes	United States of America	North America	0.5,576.78	0.2	29.47	591.37	21.80	-100.52	31.37
159	4997	Somasila	India	Asia	0.17,74.32	2.0	153.17	100.58	36.00	79.30	14.49
160	5183	Hongshan Reservoir	China	Asia	0.23,422.08	2.6	66.90	437.64	43.10	119.70	42.75
161	6583	Lake Ross	Australia	Oceania	0.11,32.61	0.8	82.00	41.77	9.80	146.74	-19.41
162	4978	Yeleru Reservoir	India	Asia	0.59,57.51	0.5	49.36	86.56	32.30	82.08	17.30
163	4696	South Surkhan Reservoir	Uzbekistan	Asia	0.34,397.8	0.8	40.26	411.41	26.20	67.63	37.83
164	5287	Zhaopingtai Reservoir	China	Asia	0.36,157.63	0.7	46.50	174.27	28.80	112.77	33.73

*The 164 reservoirs include 13 regulated natural lakes, whose IDs are 1, 6, 20, 23, 33, 37, 44, 62, 73, 102, 131, 150, and 151.

[1]*a* and *b* are the coefficients used in the A-E relationship equation: h=a*A + b, where h and A are elevation (m) and area (km^2), respectively.

Vc, *Ac*, and *Ec* represent storage, area, and elevation values at capacity, respectively.